Progressive weakening within the overriding plate during dual inward dipping subduction

Zhibin Lei[1], J. H. Davies[1]

[1]School of Earth and Environmental Sciences, Cardiff University, Cardiff, CF10 3AT, UK

Correspondence to: Zhibin Lei (leiz2@cardiff.ac.uk)

Author Twitter handles: @Lei_geodynamics

Highlights:

1. Investigate dual inward dipping subduction models implementing composite rheology

2. Self-consistently forms a fixed boundary condition and strong convective mantle flow

3. Yielding and dislocation creep are the dominant extensional deformation mechanisms

4. Strain rate-induced weakening plays a dominant role in initiating viscosity reduction

Abstract

Dual inward dipping subduction often produces complex deformation patterns in the overriding plate. However, the geodynamic process of how dual inward dipping subduction relates to this deformation remains unclear, as previous investigation all applied a compositional or Newtonian rheology. Here we apply a composite viscosity, dependent on multiple parameters, e.g., temperature, pressure, strain rate etc., in 2-D thermo-mechanical numerical modelling to investigate how dual inward dipping subduction modifies the rheological structure of the overriding plate. Three variables are investigated to understand what controls the maximum degree of weakening in the overriding plate. We find that reducing the initial length or thickness of the overriding plate, and increasing the initial thickness of the subducting plate can enhance the viscosity reduction within the overriding plate during subduction. The progressive weakening can result in a variety of stretching states ranging from 1) little or no lithosphere thinning and extension, to 2) limited thermal lithosphere thinning, and 3) localised rifting followed by spreading extension. Compared with single sided subduction, dual inward dipping subduction further reduces the magnitude of viscosity of the overriding plate. It does this by creating a dynamic fixed boundary condition for the overriding plate, and forming a stronger upwelling mantle flow which induces progressive weakening in the overriding plate. Investigation on the evolution of dominant deformation mechanism shows that dislocation and yielding contribute most to viscosity reduction, which can update to rifting and spreading extension in the overriding plate. The progressive weakening is mainly driven by the ever-increasing strain rate, which is also a precondition for initiating thermal weakening, strain localisation, lithosphere thinning and formation of new plate boundaries.

Keywords: dual inward dipping subduction; composite viscosity; strain localisation; feedback weakening; numerical modelling.

1. Introduction

Subduction can pose a fundamental tectonic overprint on the overriding plate by generating a volcanic arc (Perfit et al., 1980; Straub et al., 2020), back-arc basin (Uyeda, 1981), orogeny (Faccenna et al., 2021), or even continental breakup (Dal Zilio et al., 2018). Most subduction zones involve only one subducting slab. Here we consider multiple subducting slabs, in particular dual inward dipping subduction. Dual inward dipping subduction, or bi-vergent subduction occurs when the overriding plate is decoupled with two subducting slabs dipping towards each other. It is one of the four most commonly described subduction zones with multiple slabs, i.e., inward-dipping, same-dip, outward-dipping and oppositely dipping adjacent subduction zones (Holt et al., 2017; Király et al., 2021).

Dual inward dipping subduction zones are found in areas which exhibit complex geodynamic processes in their geological history. Seismic tomography shows that dual inward dipping subduction exists at the Caribbean plate between the Cocos slab and Lesser-Antilles subduction zone (Van Benthem et al., 2013), South-East Asia between the Philippine and the Sumatra subduction (Hall and Spakman, 2015; Huang et al., 2015; Maruyama et al., 2007), and the region between Tonga and New Hebrides subduction zones (van der Meer et al., 2018). In combination with seismic tomography, recent plate reconstructions have made it more evident that dual inward dipping subduction could have existed in some regions in the past (Faccenna et al., 2010; Hall and Spakman, 2015) constrained by suture zone petrology demonstrating the existence of paleo-subduction. A good example is the North China Craton. Suture zone studies reveal that multiple inward dipping subduction may have surrounded the North China Craton from Early Paleozoic to

Tertiary (Santosh, 2010; Windley et al., 2010).

Global strain rate map shows that a high strain rate belt is often observed in the back-arc region of the single sided subduction zone, while the distribution of high strain rate area gets complex in dual inward dipping subduction zones (Figure 2 in Kreemer et al., 2014). In detail, when the trenches between two subduction zone are far away from each other, the high strain rate belt is prone to stay with its nearest trench. While when the trenches are close to each other, a greater area of high strain rate is observed. The difference implies that dual inward dipping subduction may be more efficient in deforming the overriding plate relative to single sided subduction. Despite these observations, dual inward dipping subduction is still poorly understood in terms of how it differs from single sided subduction in deforming or weakening the overriding plate.

Numerical investigations have been conducted to understand the dynamics of dual inward dipping subduction. Research shows that the initial slab dip of the subducting plate affects the upper mantle dynamic pressure between the convergent slabs and stress state within the overriding plate (Holt et al., 2017). Varying the distance between the trenches, convergence rate, and asymmetry of subducting plates can alter the topography of the overriding plate (Dasgupta and Mandal, 2018). The thickness of the plates and the lithosphere to asthenosphere viscosity ratio are all tested to investigate their effect on the slab geometry and the magnitude of mantle upwelling flow underlying the overriding plate (Lyu et al., 2019).

These pioneering investigations show that dual inward dipping subduction can generate a variety of upper mantle flow patterns which regulate the stress state and topography of the overriding plate. However, previous models all applied a simplified constant viscosity or Newtonian rheology for both plates and convective mantle flow, i.e., the viscosity is neither temperature nor stress-dependent. Mineral deformation experiments indicate that viscosity varies as a function of multiple parameters, e.g., temperature, pressure, stress, strain rate etc. (Bürgmann and Dresen, 2008; Burov, 2011; Hirth and Kohlstedt, 2003; Karato, 2010; Lynch and Morgan, 1987). Thus, previous dual inward dipping subduction models with simplified rheology were unable to fully reflect the weakening process, e.g., high strain rate in the back-arc region, due to slab rollback and induced mantle wedge flow.

Single sided subduction models incorporating composite rheology, e.g., dislocation creep, diffusion creep, yielding etc., has improved our understanding of subduction's impact upon the overriding plate (e.g., Alsaif et al., 2020; Čížková and Bina, 2013; Garel et al., 2014; Schliffke et al., 2022; Suchoy et al., 2021). It has not been investigated before, to the best of our knowledge, in terms of which rheology law dominates the weakening process observed in the overriding plate or how different deformation mechanisms interplay with each other during subduction.

In this research, a series of 2-D thermo-mechanical models incorporating composite rheology laws are run to investigate how dual inward dipping subduction differs from single sided subduction in deforming the overriding plate. We also identify the dominant deformation mechanism that induces progressive weakening and investigate the interplay among different deformation mechanisms applied.

2. Methods

We ran the thermally-driven dual inward dipping subduction models using the code Fluidity (Davies et al., 2011; Kramer et al., 2012), a finite-element control-volume computational modelling framework, with an adaptive mesh that is set up to capture evolving changes with a maximum resolution of 0.4 km in this research.

2.1 Governing equations and rheology setup

Under the Boussinesq approximation (McKenzie et al., 1974), the equations governing thermally driven subduction process are derived from conservation of mass, momentum, and energy, for an incompressible Stokes flow

$$\partial_i u_i = 0, \tag{1}$$

$$\partial_i \sigma_{ij} = -\Delta\rho g_j, \tag{2}$$

$$\frac{\partial T}{\partial t} + u_i \partial_i T = \kappa \partial_i^2 T, \tag{3}$$

in which u, g, σ, T, κ are the velocity, gravity, stress, temperature, and thermal diffusivity, respectively (Table 1). In particular, the full stress tensor σ_{ij} consists of deviatoric and lithostatic components via

$$\sigma_{ij} = \tau_{ij} - p\delta_{ij}, \tag{4}$$

where τ_{ij} represents the deviatoric stress tensor, p the dynamic pressure, and δ_{ij} the Kronecker delta function.

The deviatoric stress tensor and strain rate tensor $\dot{\varepsilon}_{ij}$ are related according to

$$\tau_{ij} = 2\mu\dot{\varepsilon}_{ij} = \mu\left(\partial_j u_i + \partial_i u_j\right), \tag{5}$$

with μ the viscosity. The density difference due to temperature is defined as

$$\Delta\rho = -\alpha\rho_s(T - T_s), \tag{6}$$

where α is the coefficient of thermal expansion, ρ_s is the reference density at the surface temperature T_s (Table 1).

Table 1. Key parameters used in this research.

Quantity	Symbol	Units	Value
Gravity	g	$m\ s^{-2}$	9.8
Gas constant	R	$J\ K^{-1}\ mol^{-1}$	8.3145
Mantle geothermal gradient	G	$K\ km^{-1}$	0.5 (UM) 0.3 (LM)
Thermal expansivity coefficient	α	K^{-1}	3×10^{-5}
Thermal diffusivity	κ	$m^2\ s^{-1}$	10^{-6}
Reference density	ρ_s	$kg\ m^{-3}$	3300
Cold, surface temperature	T_s	K	273
Hot, mantle temperature	T_m	K	1573
Maximum viscosity	μ_{max}	$Pa \cdot s$	10^{25}
Minimum viscosity	μ_{min}	$Pa \cdot s$	10^{18}
Diffusion Creep [a]			
Activation energy	E	$kJ\ mol^{-1}$	300 (UM) 200 (LM)
Activation volume	V	$cm^3\ mol^{-1}$	4 (UM) 1.5 (LM)
Prefactor	A	$Pa^{-n}\ s^{-1}$	3.0×10^{-11} (UM) 6.0×10^{-17} (LM)
	n		1
Dislocation Creep (UM) [b]			
Activation energy	E	$kJ\ mol^{-1}$	540
Activation volume	V	$cm^3\ mol^{-1}$	12
Prefactor	A	$Pa^{-n}\ s^{-1}$	5.0×10^{-16}
	n		3.5
Peierls Creep (UM) [c]			
Activation energy	E	$kJ\ mol^{-1}$	540
Activation volume	V	$cm^3\ mol^{-1}$	10
Prefactor	A	$Pa^{-n}\ s^{-1}$	10^{-150}
	n		20
Yield Strength Law [d]			
Surface yield strength	τ_0	MPa	2
Friction coefficient	f_c		0.2
	$f_{c,weak}$		0.02 (weak layer)
Maximum yield strength	$\tau_{y,max}$	MPa	10,000

[a] The rheology parameter of diffusion creep is guided by previous mineral deformation experiments (Hirth and Kohlstedt, 2003, 1995a; Ranalli, 1995). The UM and LM stands for "upper mantle" and "lower mantle," respectively. [b] The activation parameters and stress-dependent exponent used for dislocation creep are in agreement with previous mineral deformation experiments (Hirth and Kohlstedt, 1995b). [c] The parameterisation (based on Kameyama et al., 1999) makes Peierls creep tend to be weaker than yielding in the upper mantle, thus enabling trench retreat and creating richer slab morphology in the upper mantle (Garel et al., 2014). [d] A very high maximum yield strength value is used here to ensure that yielding only dominates at the depth of crustal scale. A friction coefficient of 0.2 is following numerical models (Garel et al., 2014; Gülcher et al., 2020), and it is intermediate between lower values of previous subduction models (Crameri et al., 2012; Di Giuseppe et al., 2008) and the actual friction coefficient of the Byerlee law (Byerlee, 1978).

The key rheology difference of the model setup with previous dual inward dipping subduction models (Dasgupta and Mandal, 2018; Holt et al., 2017; Lyu et al., 2019) is that the magnitude of viscosity throughout the model can self-consistently evolve during subduction. The governing rheological laws are identical throughout the model domain, though the rheology parameters we use differ to match different deformation mechanisms potentially dominating at different depths in the Earth. In detail, a uniform composite viscosity is used to take account of four deformation mechanisms under different temperature-pressure conditions: diffusion creep, dislocation creep, Peierls mechanism, and yielding (Garel et al., 2014). The effective composite viscosity in the computational domain is given by

$$\mu = \left(\frac{1}{\mu_{diff}} + \frac{1}{\mu_{disl}} + \frac{1}{\mu_P} + \frac{1}{\mu_y}\right)^{-1}, \tag{7}$$

where μ_{diff}, μ_{disl}, μ_y define the creep viscosity following

$$\mu_{diff/disl/P} = A^{-\frac{1}{n}} exp\left(\frac{E + PV}{nRT_r}\right) \dot{\varepsilon}_{II}^{\frac{1-n}{n}}, \tag{8}$$

in which A is a prefactor, n the stress component, E the activation energy, P the lithostatic pressure, V the activation volume, R the gas constant, T_r the temperature obtained by adding an adiabatic gradient of 0.5 K/km in the upper mantle and 0.3 K/km in the lower mantle to the Boussinesq solution (Fowler, 2005), $\dot{\varepsilon}_{II}$ the second invariant of the strain rate tensor. Note that in the lower mantle only diffusion creep applies and the lower mantle is 30 times more viscous than the upper mantle. While the fourth deformation mechanism, yielding, is defined by a brittle-failure type yield-stress law as

$$\mu_y = \frac{\tau_y}{2\dot{\varepsilon}_{II}}, \tag{9}$$

with μ_y the yielding viscosity and τ_y the yield strength. τ_y is determined by

$$\tau_y = min(\tau_0 + f_c P, \tau_{y,max}), \tag{10}$$

with τ_0 the surface yield strength, f_c the friction coefficient, P the lithostatic pressure, and $\tau_{y,max}$ the maximum yield strength (Table 1).

2.2 Model setup

The computational domain is 10,000 km by 2,900 km, with x (width) coordinates and z (depth) coordinates extending from the surface to the bottom of the lower mantle (Figure 1). Such a wide domain reduces the influence of side and bottom boundary conditions (Chertova et al., 2012). The thermal boundary conditions at the surface and bottom are defined by two isothermal values: $T = T_s$ and $T = T_m$ for surface and base of lower mantle respectively, while the sidewalls are insulating. As for mechanical boundary conditions, a free-surface is applied at the top boundary to facilitate trench mobility, while the other boundaries are free-slip.

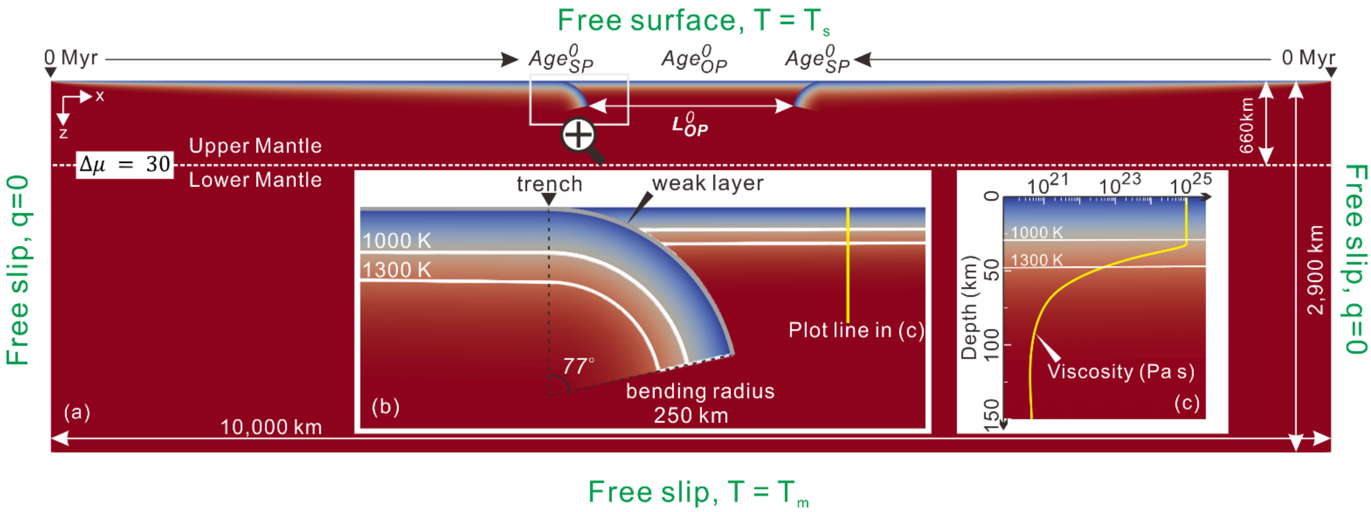

Figure 1. Dual inward dipping model geometry and initial setup illustrated with the initial temperature field as the background. (a)

The whole computational domain. Age_{SP}^0 and Age_{OP}^0 represent the initial ages of subducting plate and overriding plate at trench. The viscosity jump ($\Delta\mu$) between upper and lower mantle at 660 km transition zone is set up with a fixed value of 30. To be noted, L_{OP}^0 represents the distance between the leading tip edges of the slabs initially penetrating into the upper mantle. L_{OP}^0 roughly equals the length of the overriding plate with constant thickness, excluding the overriding plate above the interface with the bending slab. (b) Enlarged area of the trench zone where the bending slab meets the flat overriding plate. The 1100 K and 1300 K isotherms are marked in white contours. (c) Vertical profile of viscosity against depth within the overriding plate. The plot line is 400 km away from the initial trench.

To simplify the complexity of the model, a laterally symmetric dual inward dipping subduction is applied, i.e., the model is strictly symmetric along the vertical middle line of the domain (5000 km away from the side boundaries) in all aspects, e.g., the geometry and rheology properties. Age_{SP}^0 and Age_{OP}^0 represent the initial ages of subducting plate and overriding plate at the trench, where the two plates meet at the surface. Laterally on the surface, the age of the subducting plates increases linearly with their distance away from the mid-ocean ridge on either side. While vertically, the age of the plate at surface defines the initial thermal structure through a half-space cooling model (Turcotte and Schubert, 2014),

$$T(x,z) = T_s + (T_m - T_s)erf\left(\frac{z}{2\sqrt{\kappa Age^0(x)}}\right), \tag{11}$$

with x the distance away from the mid-ocean ridge, *erf* the error function, z the depth, κ the thermal diffusivity. All parameters are listed in Table 1. The whole overriding plate is set up with a constant age. Thus, the thermal structure within the overriding plate is laterally homogeneous. The bottom of thermal lithosphere is defined as the isotherm of 1300 K, where the temperature gradient starts to drop quickly (Garel and Thoraval, 2021). The initial thickness of the subducting plate (H_{SP}^0) and overriding plate (H_{OP}^0) can be calculated using

$$H_{Plate}^0 = erfinv((T_{1300K} - T_s)/(T_m - T_s)) * 2 * \sqrt{\kappa * Age_{Plate}^0(x)}, \tag{12}$$

where H_{Plate}^0 is the initial thickness of the plate thermal lithosphere and *erfinv* is the inverse error function.

The free surface boundary condition together with the mid-ocean ridge setup allows the subducting slabs, the overriding plate and therefore the trench to move freely as subduction evolves. To initiate self-driven subduction without implementing external forces, the subducting plate is set up with a bend into the mantle and an 8 km thick low-viscosity decoupling layer on the top. This weak layer has the same rheology as the rest of the domain, other than its maximum viscosity is 10^{20} Pa s, and its friction coefficient is 0.02 (i.e., an order of magnitude lower). The initial bending radius is 250 km and the slab bends over 77 degrees from the trench (Figure 1).

2.3 Model variables

Three variables are investigated here: the initial length of the overriding plate (L_{OP}^0), the initial thickness of the subducting plate (H_{SP}^0) and overriding plate (H_{OP}^0) (Table 2). These are parameters also varied in previous research and therefore will allow easier comparison. H_{SP}^0 and H_{OP}^0 are dependent on plate age and calculated using Equation (12). The magnitude of L_{OP}^0 that has been tested in previous models ranging from 500 km to 4000 km (Dasgupta and Mandal, 2018; Holt et al., 2017; Lyu et al., 2019), and the result shows that L_{OP}^0 greater than 2500 km has little impact on the result (Lyu et al., 2019). Here L_{OP}^0 is tested in the range from 500 km to 1600 km. The values of H_{SP}^0 and H_{OP}^0 that has been tested before ranges from 75-125 km and 75-150 km separately and those models suggest that H_{SP}^0 is more important in deciding the magnitude of upwelling mantle flow than H_{OP}^0 (Lyu et al., 2019). So the range of H_{SP}^0 is extended to 94-141 km (equivalent half-space age 90-200 Ma, Table 2) while the range of H_{OP}^0 is narrowed down to 67-100 km (45-100 Ma).

Table 2. List of model setup.

Model name	L_{OP}^0 (km)	H_{SP}^0 (km)	H_{OP}^0 (km)	Age_{SP}^0 (Ma)	Age_{OP}^0 (Ma)
$H_{SP}^0 = 94\ km$	500	94	67	90	45
$H_{SP}^0 = 100\ km$	500	100	67	100	45
$H_{SP}^0 = 111\ km$	500	111	67	125	45
$H_{SP}^0 = 122\ km$	500	122	67	150	45
$H_{SP}^0 = 141\ km$	500	141	67	200	45
$H_{OP}^0 = 67\ km$	500	141	67	200	45
$H_{OP}^0 = 70\ km$	500	141	70	200	50
$H_{OP}^0 = 74\ km$	500	141	74	200	55
$H_{OP}^0 = 77\ km$	500	141	77	200	60
$H_{OP}^0 = 100\ km$	500	141	100	200	100
$L_{OP}^0 = 500\ km$	500	141	67	200	45
$L_{OP}^0 = 600\ km$	600	141	67	200	45
$L_{OP}^0 = 700\ km$	700	141	67	200	45
$L_{OP}^0 = 800\ km$	800	141	67	200	45
$L_{OP}^0 = 1000\ km$	1000	141	67	200	45
$L_{OP}^0 = 1200\ km$	1200	141	67	200	45
$L_{OP}^0 = 1600\ km$	1600	141	67	200	45

Models are named with the variable tested, e.g., $H_{SP}^0 = 94\ km$ and $H_{SP}^0 = 122\ km$ corresponds to the initial subducting plate thickness of 94 km and 122 km separately, while the initial overriding plate length and thickness in both models remain the same as 500 km and 67 km.

3. Results

3.1 Varying viscosity in an evolving model: an example

The thermal-mechanical model setup of this research enables self-consistent subduction. Similar to the self-consistent single subduction numerical and analogue models, subduction initiates as negative buoyancy pulls the slab to sink into the deeper mantle, followed by a second stage when slab starts to interact with the lower mantle (e.g., Capitanio et al., 2010; Gerya et al., 2008; Schellart and Moresi, 2013). We next describe in detail the dynamic evolution of dual inward dipping subduction for the model '$L_{OP}^{0} = 1200\ km$'.

3.1.1 Subduction through the upper mantle

When slabs subduct through the upper mantle, symmetric subduction develops about the midline of the overriding plate (~5000km away from the side boundaries). As more slab is pulled into the mantle, the negative buoyancy grows gradually. It takes ~5.8 Myr before the slab starts to interact with the lower mantle (Figure 2).

Convective mantle wedge flow is generated as the subducting slab bends and sinks in the upper mantle. The size of the convective cell grows with time and forms a crescent shape as wide as ~500 km before the slab reaches the depth of lower mantle. The convective cell is composed of a narrow downwelling flow coupling close to the sinking slab and a wide upwelling flow further away. The upwelling flow fades gradually as its distance away from the subducting slab increases. In the model '$L_{OP}^{0} = 1200\ km$', the two sets of wedge flow have little interaction and can be considered as two separate units. This is because the length of the overriding plate is 1200 km, which is greater than two times the width (~500 km) of a convection cell.

The overriding plate exhibits a widespread extensional stress field as a result of continuous subduction and the induced convective mantle wedge flows. Only a limited area close to the interface with the bending slabs develops compression (Figure 2, a). The widespread extensional stress field implies that the overriding plate has an overall stretching tendency. Within the overriding plate, the governing deformation mechanism is spatially layered (Figure 2, b). At depths shallower than 30 km within the overriding plate, yielding (brittle or plastic) deformation dominates. Underlying the yielding layer lies ~10 km thick Peierls creep layer. While for depths from ~40 km to the bottom of the thermal lithosphere deformation is dominated by dislocation creep. High strain rate areas are observed within and underneath the overriding plate (Figure 2, c). The thermal thickness of the overriding plate, defined by the 1300 K isotherm contour, remains nearly constant throughout the simulation.

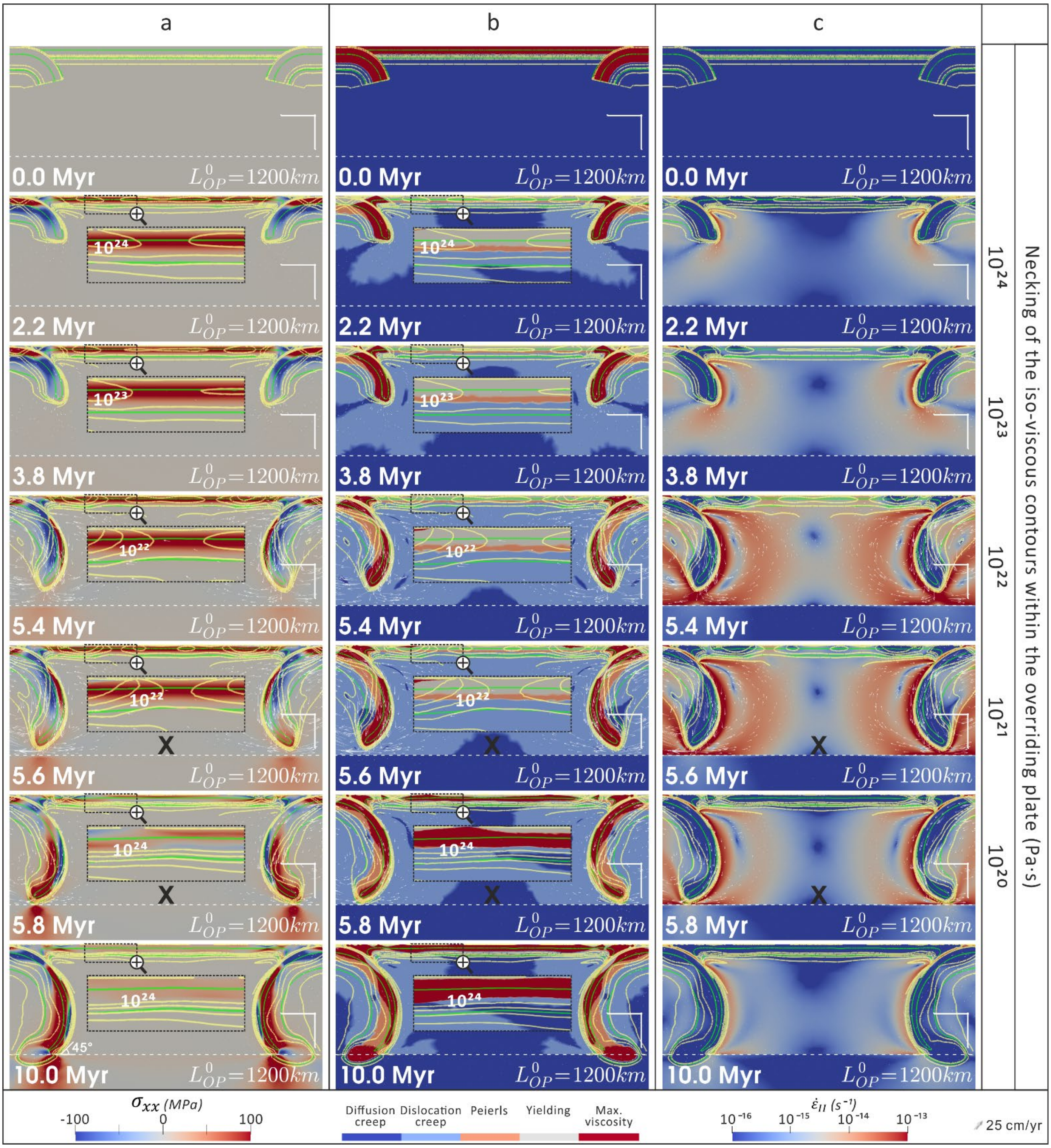

Figure 2. The Simulation screenshots of model '$L_{OP}^0 = 1200\ km$'. (a) Horizontal stress component where positive value represents stretching and negative value denotes compression. (b) Temporal evolution of the governing deformation mechanism, which is defined as the rheology law that yields the minimum magnitude of viscosity in a specific region. (c) Magnitude of second invariant of strain rate. The progressive weakening process within the overriding plate is demonstrated by the necking of the iso-viscous contours. The 5 groups of yellow contours encompassing the plates in each screenshot are iso-viscous contours of $10^{20}, 10^{21}, 10^{22}, 10^{23}, 10^{24}\ Pa \cdot s$ from outward to inward. Screenshot with a bold 'X' underlying the overriding plate means there is no necking developing in that timestep for the iso-viscous contour whose value is noted on the right-hand side, e.g., $10^{21}\ Pa \cdot s$. The two sets of green solid lines are 700 K and 1300 K isotherm contours to image the geometry of the plate. The transition zone at the depth of 660 km is marked by the horizontal white dashed line. The white right-angle scale bar lying above the right end of the transition zone represents 200 km in both directions. The bottom left corner caption shows the elapsed simulation time and bottom right corner is the name of the model.

The non-Newtonian rheology laws applied define viscosity as a function of multiple variables, e.g., temperature, lithostatic pressure, stress, strain rate etc. As subduction initiates, it creates rheology heterogeneities within what initially was a laterally homogeneous overriding plate, allowing part of it to become weaker than other parts. To visualize the variation in lithosphere viscosity, several levels of iso-viscous contours are plotted, e.g., $10^{24}, 10^{23}, 10^{22}, 10^{21}\ Pa \cdot s$ (Figure 2). Here, the overriding plate weakening is defined as the viscosity reduction process, and the weakening level is defined as the maximum order of viscosity magnitude drop. That is, weakening level 'I', 'II', 'III', 'IV' represents that the iso-viscous contour $10^{24}, 10^{23}, 10^{22}, 10^{21} Pa \cdot s$ is necked within the overriding plate respectively. It shows that the homogeneous overriding plate is gradually segmented into three strong cores connected with two low viscosity necking regions. Strain is likely to localise upon these two necking areas and continuously lower the magnitude of viscosity therein. The minimum viscosity achieved in the overriding plate for model '$L_{OP}^{0} = 1200\ km$' is 10^{21}-$10^{22}\ Pa \cdot s$ (weakening level 'III'). The distance between these two necking regions is ~620 km (Figure 2, a, 3.8Myr). These necking regions match well with the high strain rate areas developed in the overriding plate. The initial result suggests that high strain rate may play an important role in softening the overriding plate during dual inward dipping subduction.

3.1.2 Subduction into the lower mantle

Due to the viscosity jump at transition zone, subduction approaching the lower mantle would experience a short period of deceleration, where mobility of the slab tends to slow down and the induced mantle wedge flow becomes mild. Meanwhile, the necking of the iso-viscous contours is reversed by a cooling and strengthening process within the overriding plate (Figure 2). At the end of the 10 Myr simulation, the dip between the top of bending slab and the transition zone is ~45° and the total trench retreat is ~100 km.

3.2 Length of the overriding plate

The first series of models investigate decreasing the initial length of the overriding plate (L_{OP}^{0}) from 1600 km to 500 km, while keeping the initial thickness of the subducting and overriding plate as 141 km and 67 km separately. As L_{OP}^{0} decreases, the two symmetric subducting slabs become closer. The two separate convective mantle wedge flows start to combine with each other and form a stronger joint upwelling flow underneath the overriding plate (Figure 3). Consequently, as L_{OP}^{0} is reduced, the two separate necking areas within the overriding plate get closer and merge into a single one in the end. Also as L_{OP}^{0} is reduced it takes less time to lower each level of viscosity within the overriding plate. Besides, the progressive weakening process can go further and neck the $10^{21}\ Pa\ s$ iso-viscous contour (weakening level 'IV') when L_{OP}^{0} reaches <= 800 km, initiating significant lithosphere thinning and even rifting or spreading extension within the overriding plate (Figure 3, b-c). In this paper, we define rifting as a process where plate's thermal thickness reduces to ~0 km. It is noted that the rifting process in this research does not include melting behaviour. The significant extension usually lasts less than 1 Myr before it gradually stops after the slab reaches the depth of the lower mantle, but it causes substantial changes to the dual inward dipping subduction system. For example, significant slab rollback starts to develop, creating a flattening slab geometry in the upper mantle and steepening dip angle (45° to 75°, Figure 3) at the transition zone depth by the end of the 10 Myr simulation.

It is noted that the continuous thinning of the thermal lithosphere only initiates when the iso-viscous contour of $10^{21}\ Pa \cdot s$ starts to neck, indicating a good coupling of the thermal lithosphere and the rheology boundary layer (usually defined as the depth of $10^{21}\ Pa \cdot s$) in the model. All models necking $10^{21}\ Pa \cdot s$ will continue to neck lower magnitudes of viscosity, e.g., $10^{20}, 10^{19}\ Pa \cdot s$. Simultaneously, the upwelling hot mantle flow can then ascend to fill the thinning region and create a new plate boundary (rifting extension) or even new sea floor (spreading extension) after it ascends to the surface. Thus, the ability to neck $10^{21}\ Pa \cdot s$ (or not) can be used as a key diagnostic to predict whether a new spreading ridge (new plate boundary) develops within the overriding plate (or just limited thinning).

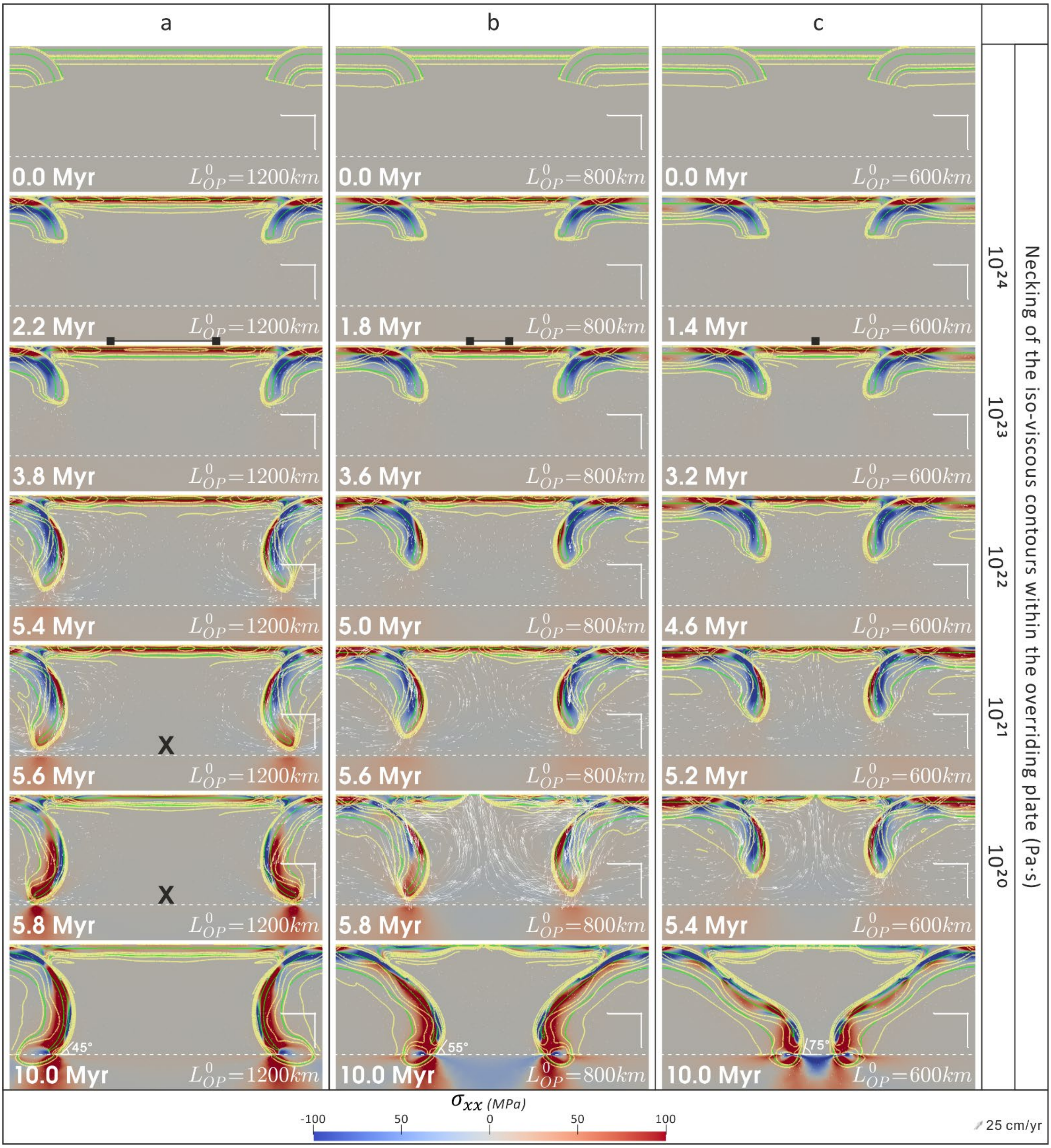

Figure 3. Progressive weakening of the overriding plate during dual inward dipping subduction with decreasing length of the overriding plate, (a) model '$L_{OP}^{0} = 1200\ km$', (b) model '$L_{OP}^{0} = 800\ km$', (c) model '$L_{OP}^{0} = 600\ km$'. The location of necked regions in the overriding plate are marked with black squares. A detailed explanation of the contours and symbols could be found in the caption of Figure 2.

To take a closer look at the extension behaviour within the overriding plate, we plot the evolving magnitude of viscosity at 5km depth (Figure 4). The filled region in the figure represents the overriding plate, therefore its widening represents extension within the overriding plate. As the initial length of the overriding plate (L_{OP}^0) decreases from 1600 km to 500 km, the total extension in the 10 Myr simulations increases from ~100 km (Figure 4, a-c) to 400-600 km (Figure 4, d-g). In detail, it is noted that extensional behaviour only become observable after the iso-viscous contour of $10^{23}\ Pa \cdot s$ is necked, i.e., after weakening level 'II' is achieved. Extension combining with lithospheric thinning only becomes significant when the iso-viscous contour $10^{21}\ Pa \cdot s$ is necked, i.e., when weakening level 'IV' is achieved. The highest weakening level achieved within the overriding plate increases from 'II' ($L_{OP}^0 = 1600\ km$) to 'III' ($L_{OP}^0 = 1000\ km$) and on to 'IV' ($L_{OP}^0 \leq 800\ km$). During the spreading extension period, a highly centralised spreading centre (Figure 4, d,f-g) is observed in the middle of the overriding plate (Figure 4, d, f-g), while multiple spreading centres are observed to accommodate the extension in model '$L_{OP}^0 = 700\ km$' (Figure 4, e).

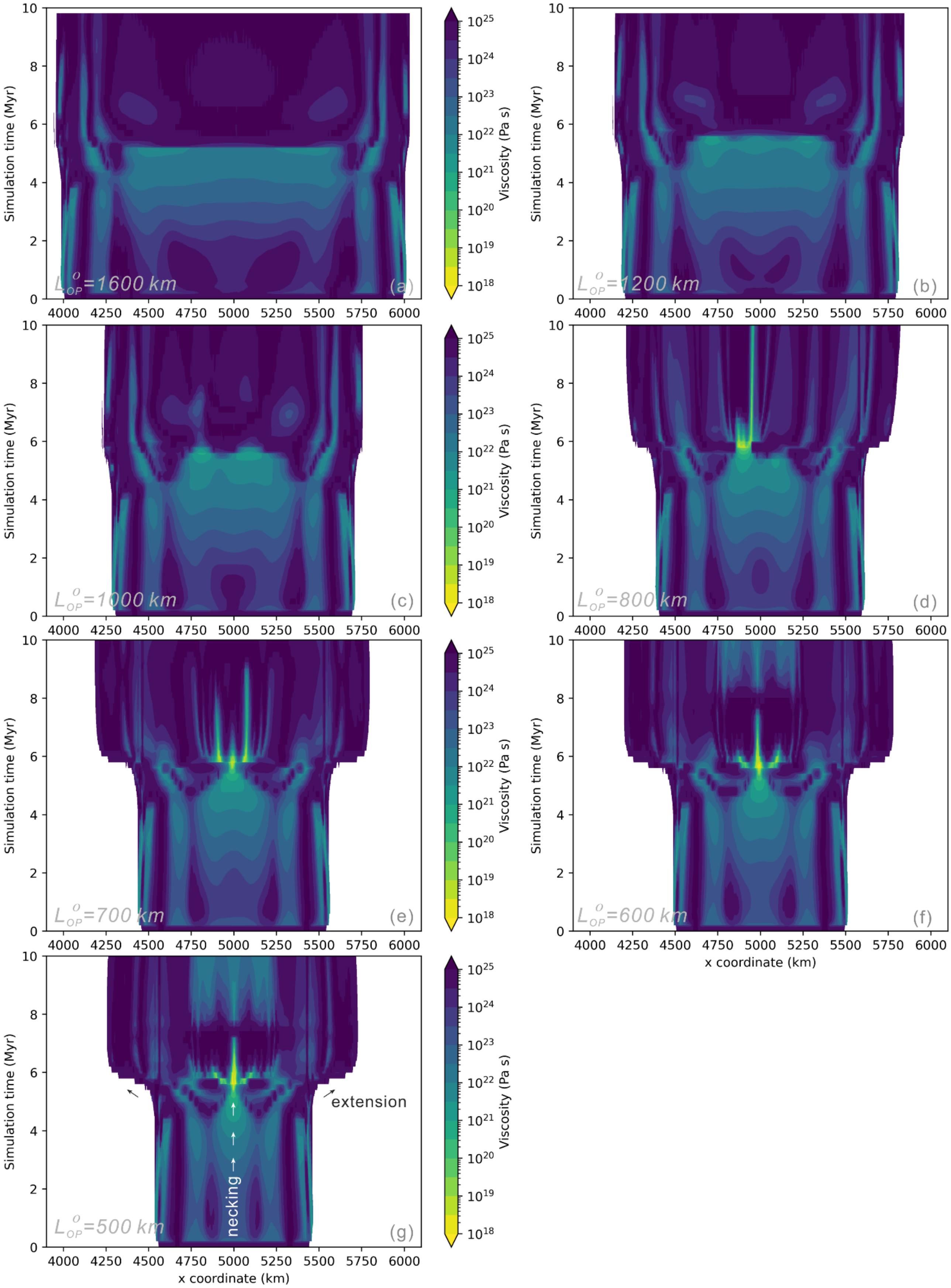

Figure 4. Temporal evolution of viscosity magnitude along the depth of 5 km within the overriding plate for models with different length of the overriding plate. (a) Model '$L^0_{OP} = 1600\ km$'. (b) Model '$L^0_{OP} = 1200\ km$'. (c) Model '$L^0_{OP} = 1000\ km$'. (d) Model '$L^0_{OP} = 800\ km$'. (e) Model '$L^0_{OP} = 700\ km$'. (f) Model '$L^0_{OP} = 600\ km$'. (g) Model '$L^0_{OP} = 500\ km$'. All models have the same setup of H^0_{SP} (141 km) and H^0_{OP} (67 km). The edge of the filled contour in the lateral direction represents the interface between the overriding plate and subducting plate. The white arrows display the necking process of the overriding plate.

3.3 Thickness of the overriding plate

The second series of models increase the initial thermal thickness (defined by the 1300 K contour) of the overriding plate (H_{OP}^0) from 67 km to 100 km (Figure 5), while keeping the subducting plate's thickness (H_{SP}^0) and the length of the overriding plate (L_{OP}^0) constant (Table 2). As H_{OP}^0 increases, the maximum weakening level developed within the overriding plate drops from 'IV' ($H_{OP}^0 = 67\ km$) to 'III' ($H_{OP}^0 = 74\ km$) and less than 'I' ($H_{OP}^0 = 100\ km$). The time it takes to lower each order of viscosity magnitude increases, indicating a slower progressive weakening.

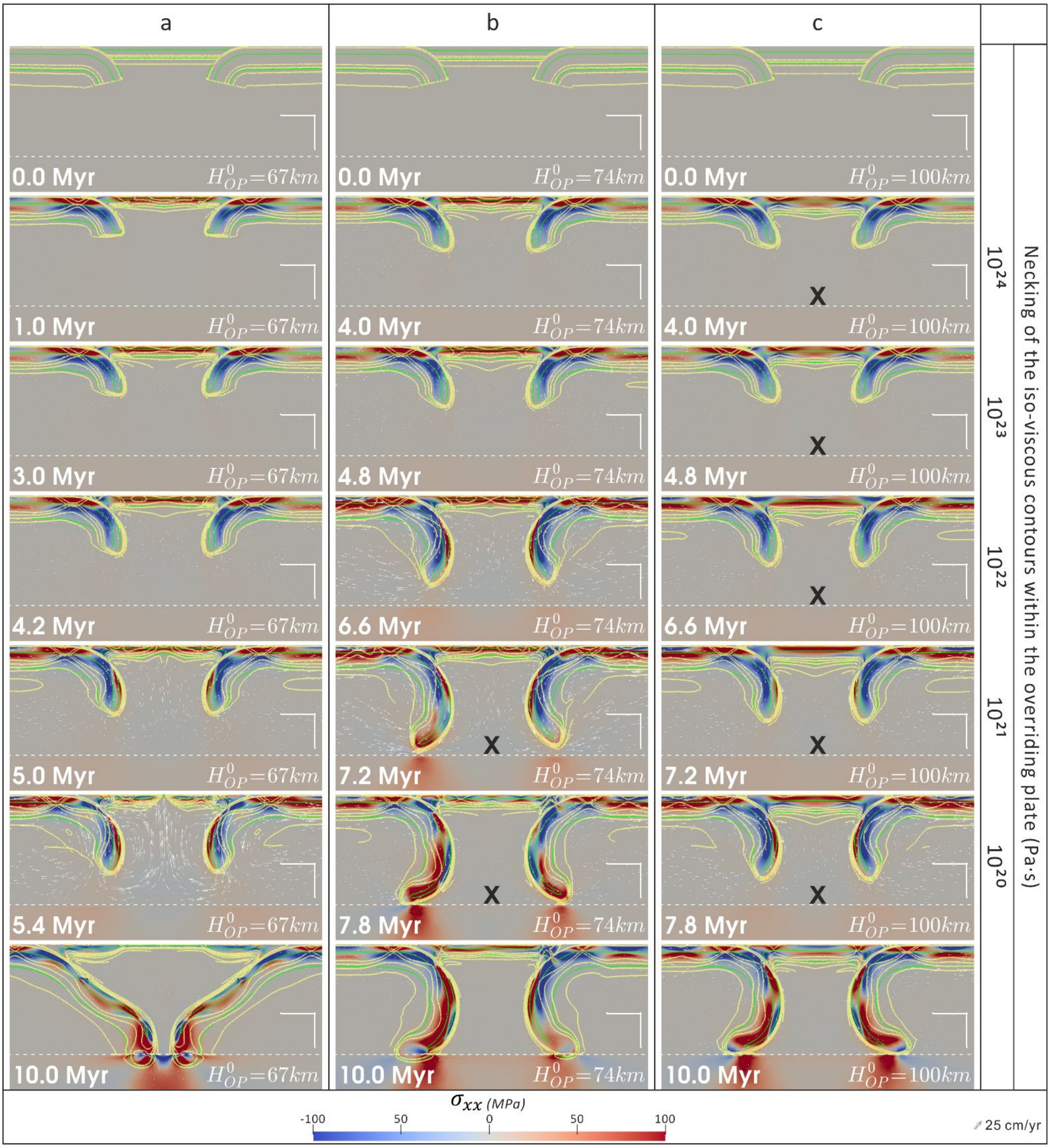

Figure 5. Progressive weakening, illustrated by visualising the stress σ_{xx}, of the overriding plate during dual inward dipping subduction with increasing thickness of the overriding plate, (a) model '$H^0_{OP} = 67\ km$', (b) model '$H^0_{OP} = 74\ km$' and (c) model '$H^0_{OP} = 100\ km$'. A detailed explanation of the contours and symbols could be found in the caption of Figure 2.

Besides, the total extension decreases from ~600 km ($H^0_{OP} = 67\ km$, Figure 6, a) to ~350 km ($H^0_{OP} = 70\ km$, Figure 6, b) and ultimately to ~0 km ($H^0_{OP} = 100\ km$, Figure 6, c-e). The maximum viscosity reduction in both the primary and secondary necking regions decreases as H^0_{OP} increases, while the lateral distance away from the trench of necking regions are equal, showing no correlation with H_{OP}^0.

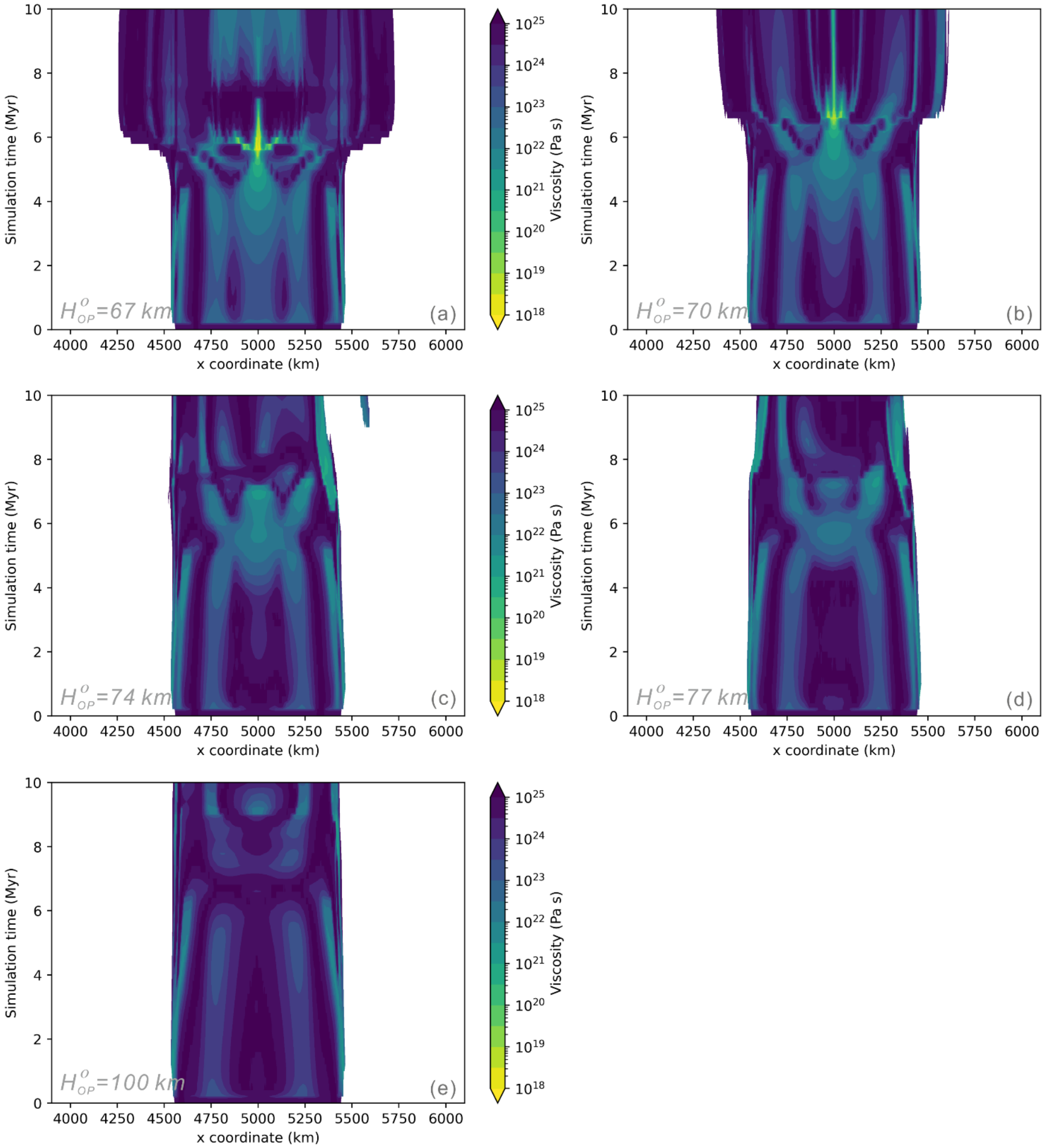

Figure 6. Temporal evolution of viscosity along a horizontal line at the depth of 5km in the overriding plate. (a) Model '$H_{OP}^0 = 67\ km$'. (b) Model '$H_{OP}^0 = 70\ km$'. (c) Model '$H_{OP}^0 = 74\ km$'. (d) Model '$H_{OP}^0 = 77\ km$'. (e) Model '$H_{OP}^0 = 100\ km$'. All models have the same H_{SP}^0 (141 km) and L_{OP}^0 (500 km). The edge of the contour filling in the lateral direction represents the interface between the overriding plate and subducting plate.

To investigate the details of the progressive weakening in the necking region, 5 diagnostics are evaluated along the vertical slice in the middle of the overriding plate (5000 km away from both side boundaries). This is where the necking belt develops in models with L_{OP}^{0} of 500 km. The diagnostics are integrated along the vertical slice and then divided by the thickness of the plate (Equation (13)),

$$\bar{D} = \frac{1}{H_{OP}} \int_{0}^{H_{OP}} D \ dy, \tag{13}$$

in which D represent the diagnostic. The averaged results include magnitude of viscosity ($\bar{\mu}$), second invariant of strain rate ($\overline{\dot{\varepsilon}_{II}}$), lithosphere thickness ($\overline{d_{OP}}$), horizontal stretching stress component ($\overline{\sigma_{xx}}$), vertical velocity component ($\overline{v_y}$), and temperature ($\bar{T}$).

Take the model '$H_{OP}^{0} = 67\ km$' for example (blue line), the evolution of the 6 diagnostics during dual inward dipping subduction is analysed (Figure 7). There is gradual increase of $\overline{\dot{\varepsilon}_{II}}$ and $\overline{\sigma_{xx}}$, and gradual decrease of $\bar{\mu}$ during the simulation between 1 Myr to 4 Myr. While $\overline{d_{OP}}$, $\bar{T}$ and $\overline{v_y}$ remains nearly constant. From 4 Myr to 5 Myr, $\overline{\dot{\varepsilon}_{II}}$ and $\bar{\mu}$ keep a similar slope trend as before. But $\overline{\sigma_{xx}}$ stops increasing and starts to decrease gently. $\overline{v_y}$ starts to increase and $\overline{d_{OP}}$ starts to decrease, while $\bar{T}$ experiences little change. During the rifting and spreading extension between 5 Myr to 6 Myr, all diagnostics are varying more rapidly, with $\bar{\mu}$, $\overline{d_{OP}}$ and $\overline{\sigma_{xx}}$ dropping and $\overline{\dot{\varepsilon}_{II}}$, $\overline{v_y}$ and $\bar{T}$ climbing steeply. Afterwards, the weakening process is replaced by a strengthening process where $\bar{\mu}$ and $\overline{d_{OP}}$ both increase while $\overline{\dot{\varepsilon}_{II}}$ and $\overline{v_y}$ decrease gradually.

As the thickness of the overriding plate increases from 67 km to 100 km, the magnitude of viscosity drop in the necking area decreases. In detail, the plotting (Figure 7, a, grey dashed line) shows that if $\bar{\mu}$ in the necking area of the overriding plate is above $\sim 2 \times 10^{22}\, Pa \cdot s$, there is no lithospheric thinning in the necking region (Figure 7, c, purple and red lines). In the timesteps when $\bar{\mu}$ is in the range of $10^{21} - 2 \times 10^{22}\, Pa \cdot s$, thinning starts to build up, but it's not weak enough to have rifting extension (Figure 7, c, green line). Only when the $\bar{\mu}$ drops below $10^{21}\, Pa \cdot s$ does significant thinning develop within the overriding plate (Figure 7, c, blue and orange lines). The results of $\bar{\mu}$ confirms that the iso-viscous contour $10^{21}\, Pa \cdot s$ can be used to predict if rifting or spreading extension develops during the dual inward dipping subduction. It also reveals a more precise maximum viscosity below which the thinning of lithosphere develops.

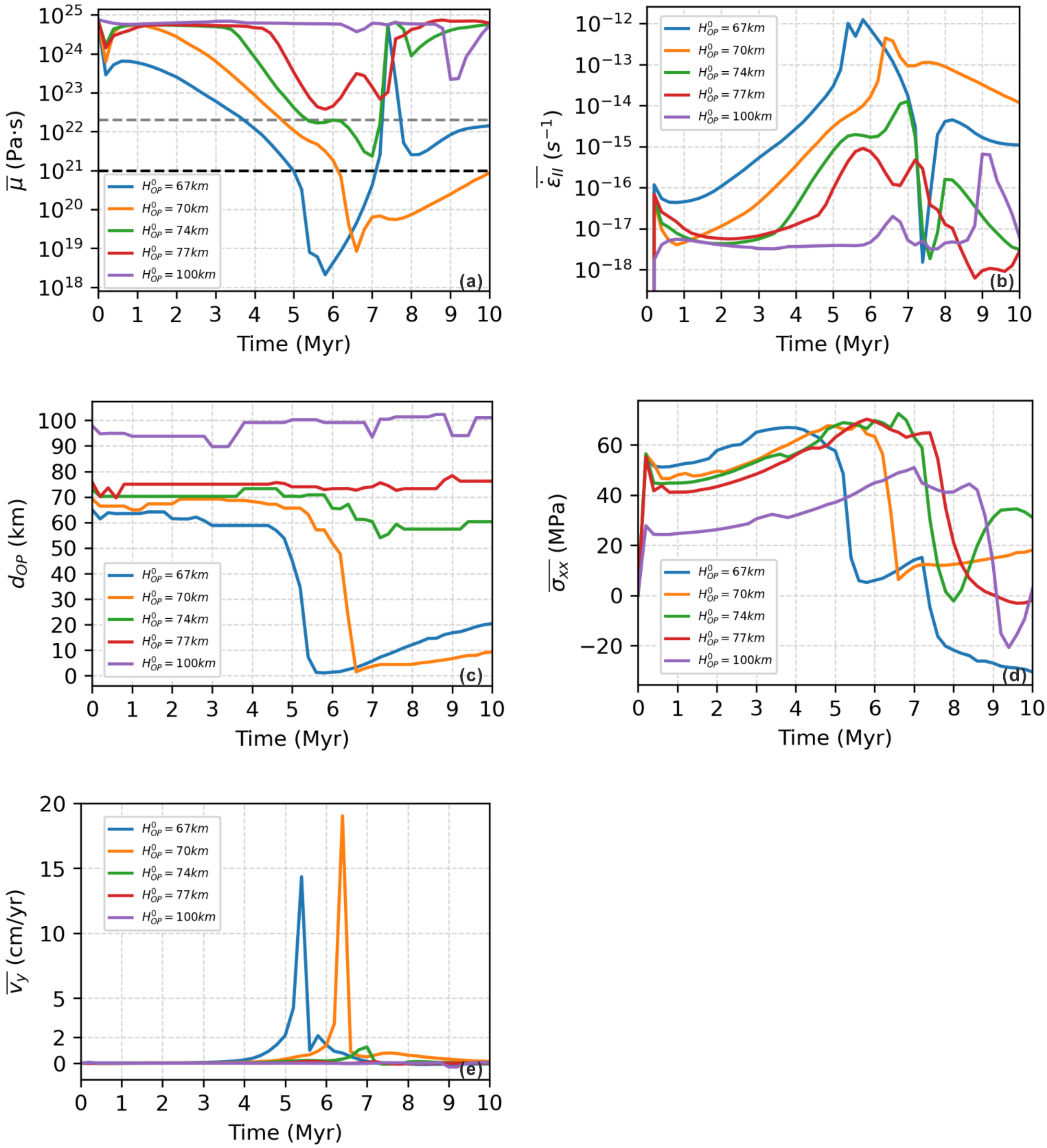

Figure 7. Temporal evolution of averaged diagnostics along the vertical slice in the middle of the overriding plate, (a) viscosity ($\overline{\mu}$), (b) second invariant of strain rate ($\overline{\dot{\varepsilon}_{II}}$), (c) lithosphere thickness ($\overline{d_{OP}}$), (d) horizontal stretching stress component ($\overline{\sigma_{xx}}$) and (e) vertical velocity component ($\overline{v_y}$). Positive value of $\overline{v_y}$ represent upward motion.

3.4 Thickness of the subducting plate

The third series of models investigate increasing the initial thermal thickness (again as defined by the 1300 K contour) of the subducting plate (H_{SP}^0) from 94 km to 141 km (Figure 8), while keeping the overriding plate's thickness (H_{OP}^0) and the length of the overriding plate (L_{OP}^0) constant. As H_{SP}^0 increases, the maximum weakening level developed within the overriding plate increases from 'I' ($H_{SP}^0 = 94\ km$) to 'III' ($H_{SP}^0 = 122\ km$) and 'IV' ($H_{SP}^0 = 141\ km$). The time it takes to lower each order of viscosity magnitude decreases, indicating a faster progressive weakening.

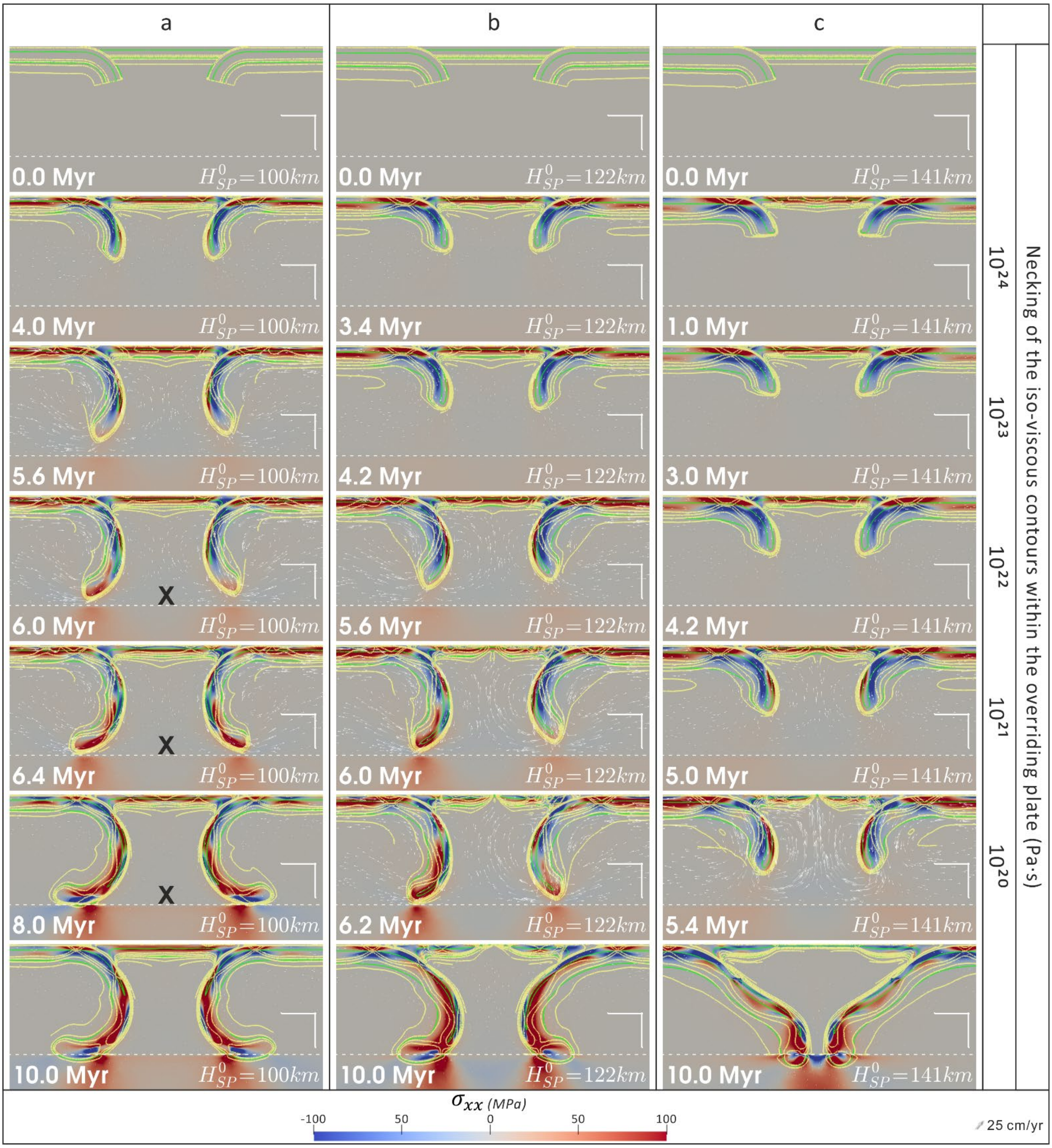

Figure 8. Progressive weakening of the overriding plate during dual inward dipping subduction with increasing age of the subducting plate. (a) Model '$H_{SP}^0 = 100\ km$'. (b) Model '$H_{SP}^0 = 122\ km$'. (c) Model '$H_{SP}^0 = 141\ km$'. A detailed explanation of the contours and symbols could be found in the caption of Figure 2.

Besides, the total extension increases from ~0 km ($H_{SP}^0 \leq 111\ km$, Figure 9, a-c) to ~200 km ($H_{SP}^0 = 122\ km$, Figure 9, d) and ultimately to ~600 km ($H_{SP}^0 = 141\ km$, Figure 9, e). The maximum viscosity reduction in both the primary and secondary necking regions increases as H_{SP}^0 increases, while the lateral distance away from the trench of necking regions are equal, showing little correlation with H_{SP}^{0}.

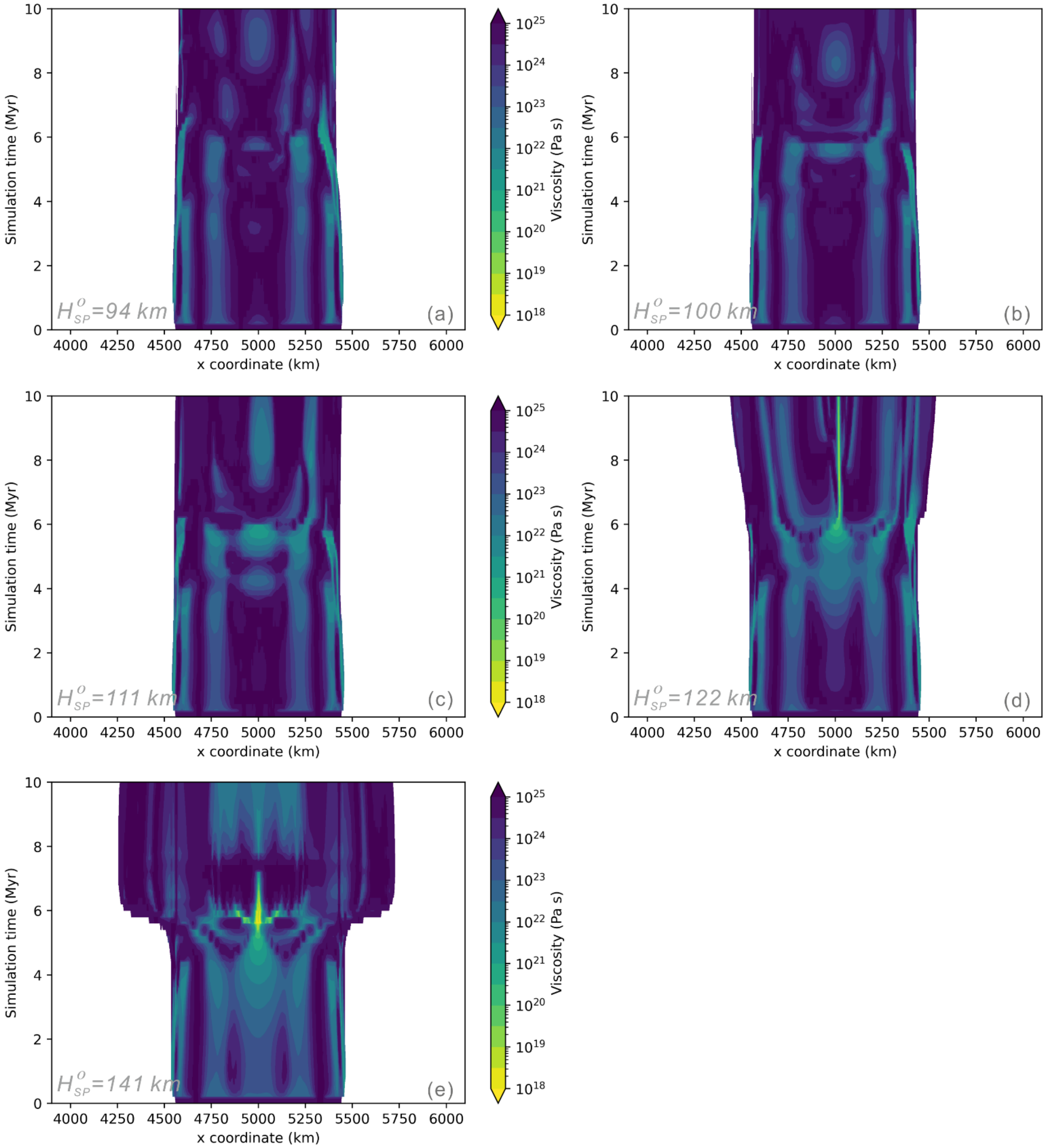

Figure 9. Temporal evolution of viscosity along a horizontal line at the depth of 5km in the overriding plate. (a) Model '$H_{SP}^{0} = 94\ km$'. (b) Model '$H_{SP}^{0} = 100\ km$'. (c) Model '$H_{SP}^{0} = 111\ km$'. (d) Model '$H_{SP}^{0} = 122\ km$'. (e) Model '$H_{SP}^{0} = 141\ km$'. Both models have the same H_{OP}^{0} (67 km) and L_{OP}^{0} (500 km). The edge of the contour filling in the lateral direction represents the interface between the overriding plate and subducting plate.

3.5 Regime of stretching state

A variety of deformation patterns and stretching state within the overriding plate have been observed when varying L_{OP}^0, H_{OP}^0 and H_{SP}^0. Several diagnostics are reported together to quantify the deformation developed within the overriding plate during the 10 Myr simulation (Table 3). The detail of each diagnostic is described as follows.

Table 3. Summary of diagnostics for all models. For further description of the diagnostics please see the main text.

Model name	weakening level	t_{rift} (Myr)	t_{660} (Myr)	l_{n2n} (km)	total strain
$H_{SP}^0 = 94\ km$	I	-	6.6	0	1%
$H_{SP}^0 = 100\ km$	III	-	6.4	0	2%
$H_{SP}^0 = 111\ km$	III	-	6.4	0	21%
$H_{SP}^0 = 122\ km$	IV	6.2	6.4	0	110%
$H_{SP}^0 = 141\ km$	IV	5.4	6.0	0	2800%
$H_{OP}^0 = 67\ km$	IV	5.4	6.0	0	2800%
$H_{OP}^0 = 70\ km$	IV	6.4	6.6	0	1300%
$H_{OP}^0 = 74\ km$	III	-	7.2	0	30%
$H_{OP}^0 = 77\ km$	II	-	7.6	0	4%
$H_{OP}^0 = 100\ km$	I	-	8.8	0	1%
$L_{OP}^0 = 500\ km$	IV	5.4	6.0	0	2800%
$L_{OP}^0 = 600\ km$	IV	5.4	6.0	0	690%
$L_{OP}^0 = 700\ km$	IV	5.6	6.0	130	630%
$L_{OP}^0 = 800\ km$	IV	5.8	6.0	231	14% [a]
$L_{OP}^0 = 1000\ km$	III	-	6.0	282	15%
$L_{OP}^0 = 1200\ km$	III	-	5.8	621	11%
$L_{OP}^0 = 1600\ km$	II	-	5.4	937	4%

[a] The total strain listed here is calculated along the middle vertical slice (5000 km away from side boundaries). For models $L_{OP}^0 \geq 800\ km$, the necking zones are away from this middle vertical slice. So, the total strain could be underestimated for these models. Considering that only model '$L_{OP}^0 = 800\ km$' achieved weakening level 'IV', the corrected total strain along its necking zone is ~600%. While the underestimation for other models is moderate and will not change the conclusion of this research.

As introduced in section 3.1.1, weakening levels 'I', 'II', 'III', 'IV' are determined by the minimum viscosity contour which is necked in the overriding plate during subduction. The higher the weakening level, the stronger the localised rheology modification observed within the overriding plate. All three groups of dual inward dipping subduction models manage to yield a variety of weakening levels in the overriding plate (Figure 10, a-c).

t_{rift} indicates the timestep when the overriding plate develops rifting extension (weakening level 'IV'), and a void value means that model fails to generate rifting extension within the overriding plate. It shows that only models achieving weakening level 'IV' develop rifting extension. t_{rift} increases with thicker or longer overriding plate, and decreases with thicker subducting plate.

t_{660} equals how much time the subducting plate (defined by its 1300 K isotherm) takes to sink to the depth of 660km. It is most sensitive to the variation of H_{OP}^{0}, while varying L_{OP}^{0} and H_{SP}^{0} generates less than ~1 Myr difference of t_{660} compared with a ~3 Myr difference when modifying H_{OP}^{0}.

l_{n2n} is the horizontal distance between necking centres which may develop rifting extension during dual inward dipping subduction, i.e., secondary necking regions are excluded. The value of l_{n2n} is 0 km if there is only one necking centre within the overriding plate. l_{n2n} starts to increase with L_{OP}^{0} when L_{OP}^{0} is greater than ~700 km. l_{n2n} in Table 3 is recorded at the timestep of 4.4 Myr. It should be noted that, l_{n2n} may vary with time and the difference is at most ~250 km (Figure 4).

Total strain is calculated by integrating the average strain rate ($\overline{\dot{\varepsilon}_{II}}$ based on Equation (13)) with time throughout the 10 Myr simulation. All three groups of models generate a variety of total strain at the end of the simulation (Figure 10, d-f). For all models that develop rifting extension, the total strain is greater than 100%. Total strain in the range of 5% to 100% is observed from limited thinning up to significant extension. For models where the total strain is less than 5%, the weakening deformation is hardly observable in the overriding plate.

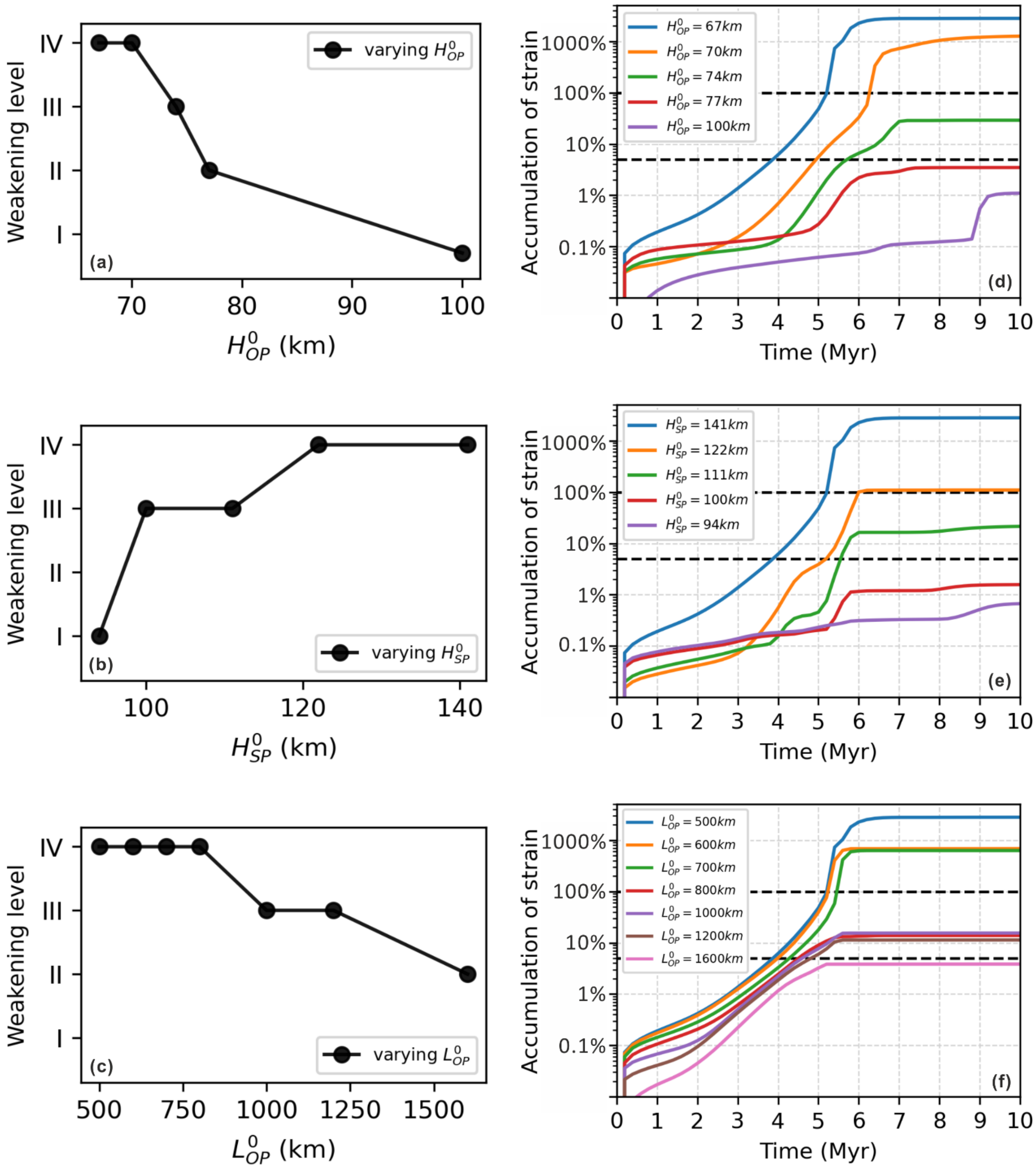

Figure 10. Key diagnostics used to characterise the rheology modification within the overriding plate. (a-c) Weakening level developed within the overriding plate. (d-f) Accumulation of strain in the middle of the overriding plate (5000 km away from the side boundaries).

By combing all the qualitative and quantitative diagnostics presented in these results, we classify three stretching states: 1) little or no lithosphere thinning and extension, discriminated by low weakening level up to level 'II', little total strain up to 5% and almost no thermal lithosphere thinning in the necking area; 2) limited lithosphere thinning and extension, identified by medium weakening level up to level 'III', medium total strain up to 30%, and limited thermal lithosphere thinning, e.g., ~15 km thinning for model '$H_{OP}^{0} = 74\,km$' (Figure 7, c); 3) rifting and spreading extension, characterised by high weakening level up to level 'IV', high total strain over 100%, and total thinning of the thermal lithosphere during rifting extension.

4. Discussion

The results show that dual inward dipping subduction can induce progressive weakening within a uniform overriding plate. With appropriate conditions, tested in this research, e.g., thick enough H_{SP}^{0}, thin enough H_{OP}^{0}, short enough L_{OP}^{0}, different levels of stretching state, ranging from no thinning nor extension to rifting and spreading extension, can develop within the homogeneous overriding plate. The role that dual inward dipping subduction plays during the progressive weakening and the origin of the softening process are worth discussion.

4.1 The role dual inward dipping subduction plays

4.1.1 Creating fixed trailing boundary condition for the overriding plate

Due to the symmetric model setup, subducting plates on both sides are prone to advance or retreat simultaneously. This creates roughly equal, symmetric and competing force from both ends of the overriding plate during subduction. As a result, the mobility of the overriding plate is inhibited, as indicated by the low velocity (<1 cm/yr, white contour) region within the overriding plate (Figure 11, a-c). It would be as if the mechanical boundary condition on the overriding plate was fixed. As the overriding plate keeps weakening during dual inward dipping subduction, divergent velocity difference can build up within the overriding plate, indicating initiation of extension (Figure 11, b-c).

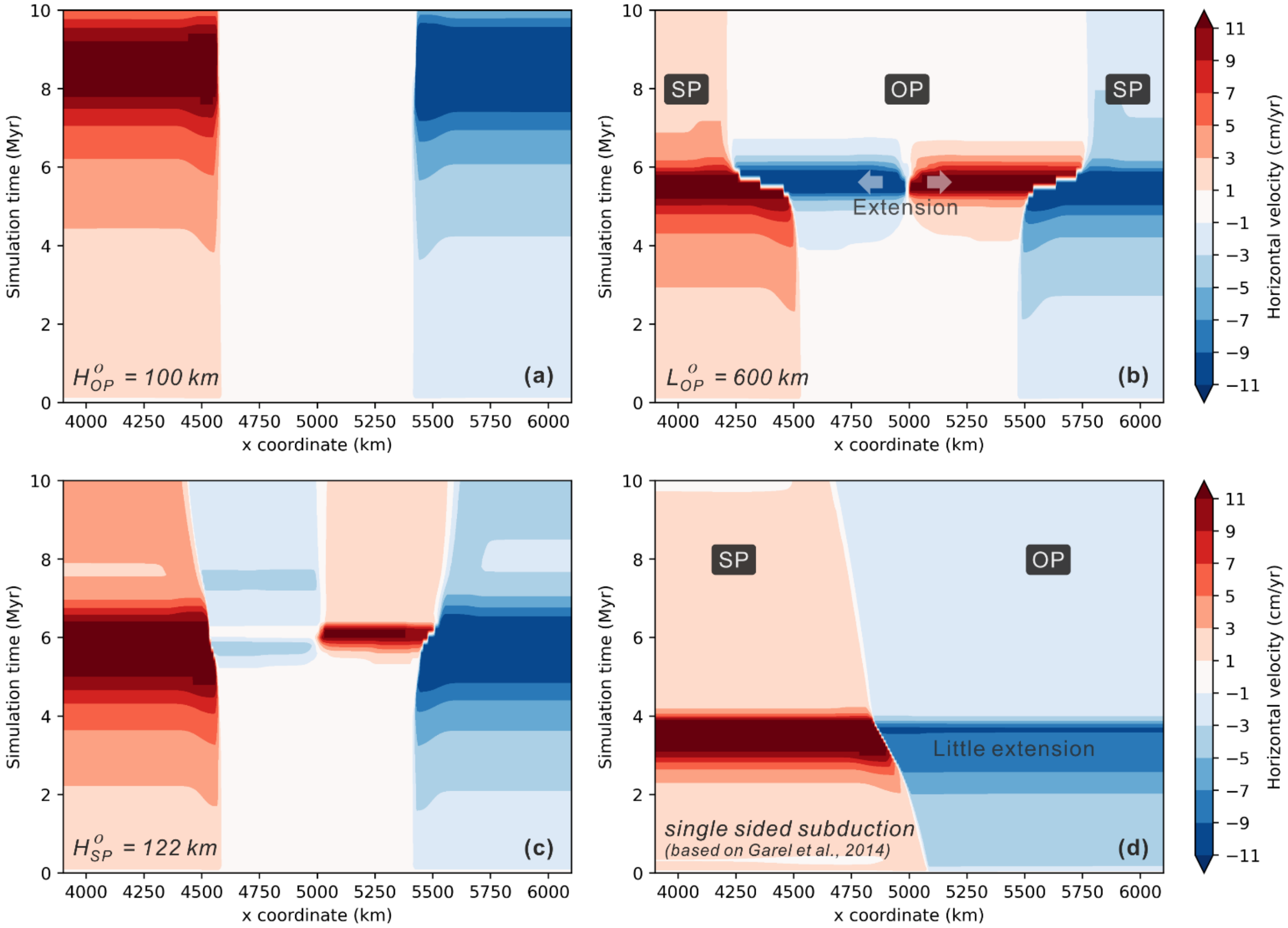

Figure 11. Temporal evolution of horizontal velocity component along a lateral slice, x coordinate from 3900km to 6100 km, at the depth of 20 km from the surface. (a) model '$H^0_{OP} = 100\ km$', (b) model '$L^0_{OP} = 600\ km$', (c) model '$H^0_{SP} = 122\ km$', (d) single sided subduction with a mobile overriding plate referring to (b) model '$L^0_{OP} = 600\ km$'. The contour filling represents the variation of horizontal component of velocity vector throughout the 10 Myr simulation. Positive value means right-ward motion and negative value is left-ward motion. The white area represents that the plate is nearly stagnant. And the edge of the white area marks the interface between the subducting plate and overriding plate or rifting and spreading centre within the overriding plate. SP and OP are short for subducting plate and overriding plate separately.

Previous studies on single-sided subduction cases have implied that the mobility of the overriding plate plays an important role in producing extension, especially in the back-arc region of the overriding plate. A mobile overriding plate can move as a whole to inhibit the build-up of deviatoric stress within the plate (Capitanio et al., 2010; Chen et al., 2016; Garel et al., 2014; Holt et al., 2015;

Nakakuki and Mura, 2013), while the immobile overriding plate can facilitate strain localisation which accounts for the increased degree of deformation in the overriding plate compared with mobile plates (Capitanio et al., 2010; Chen et al., 2016; Erdős et al., 2021; Nakakuki and Mura, 2013; Yang et al., 2019).

To investigate the role of fixed trailing boundary condition in promoting extension, we consider a single sided subduction (SSS) with a free and mobile overriding plate, based on previous single subduction research (Garel et al., 2014). The SSS has the same parameter with dual inward dipping subduction model '$L_{OP}^{0} = 600\ km$' in every aspect, e.g., rheology, initial subduction plate thickness (141 km) and initial overriding plate thickness (67 km) at the trench, except that there is only one subducting plate and the overriding plate holds a mobile side boundary. The results show that much less extension, evidenced by the magnitude of divergent velocity difference, is observed in the overriding plate of SSS model (Figure 11, d) relative to that in the model '$L_{OP}^{0} = 600\ km$' (Figure 11, b). Thus, the lack of mobility of the overriding plate plays a key role in promoting the degree of weakening during dual inward dipping subduction.

4.1.2 Stronger poloidal return flow

Our results show that varying the size of the overriding plate can affect the degree of extension within the overriding plate. Previous research shows that subduction can induce poloidal mantle return flow, which has been suggested to account for extensional deformation within the overriding plate, e.g., back-arc extension, supercontinent breakup (Chen et al., 2016; Dal Zilio et al., 2018; Erdős et al., 2021; Gerardi and Ribe, 2018; Sleep and Toksöz, 1971). Previous research also implies that, a) increasing the thickness of the subducting plate (H_{SP}^{0}) can increase the net negative buoyancy thus leading to a stronger poloidal flow (Garel et al., 2014); b) lowering the thickness of the overriding plate (H_{OP}^{0}) can not only increase the net negative buoyancy by increasing the hanging slab area in the upper mantle, but also reduces the dissipation during subduction along the interface between two plates (Erdős et al., 2021). These two mechanisms also come into play for dual inward dipping subduction models.

In addition, dual inward dipping subduction models can yield a third way to strengthen the return flow. This is by combining the two separate poloidal convection flows, one from each subducting plate, as the length of the overriding plate (L_{OP}^{0}) shortens (Figure 3). This is shown for example by the velocity variation in both the horizontal (v_x) and vertical (v_y) direction at the depth of 75 km (Figure 12). For all dual inward dipping subduction models, the magnitude of v_x decreases gradually from ~2.5 cm/yr in the mantle wedge corner to 0 cm/yr underlying the middle part (~5000 km away from side boundaries) of the overriding plate (Figure 12, a). As L_{OP}^{0} changes, models with shorter overriding plate have greater v_x gradient along the lateral slice (Figure 12, b). The maximum magnitude of v_y increases from ~0.25 cm/yr to ~1.3 cm/yr, implying a faster upwelling flow, as the length of the overriding plate (L_{OP}^{0}) shortens (Figure 12, c-d). It is also noted that the necking area developed within the overriding plate (e.g., Figure 3) lies right above the maximum upwelling component of the return flow (Figure 12, c). The observation indicates a spatial correlation between the stronger poloidal return flow and the progressive weakening in the overriding plate.

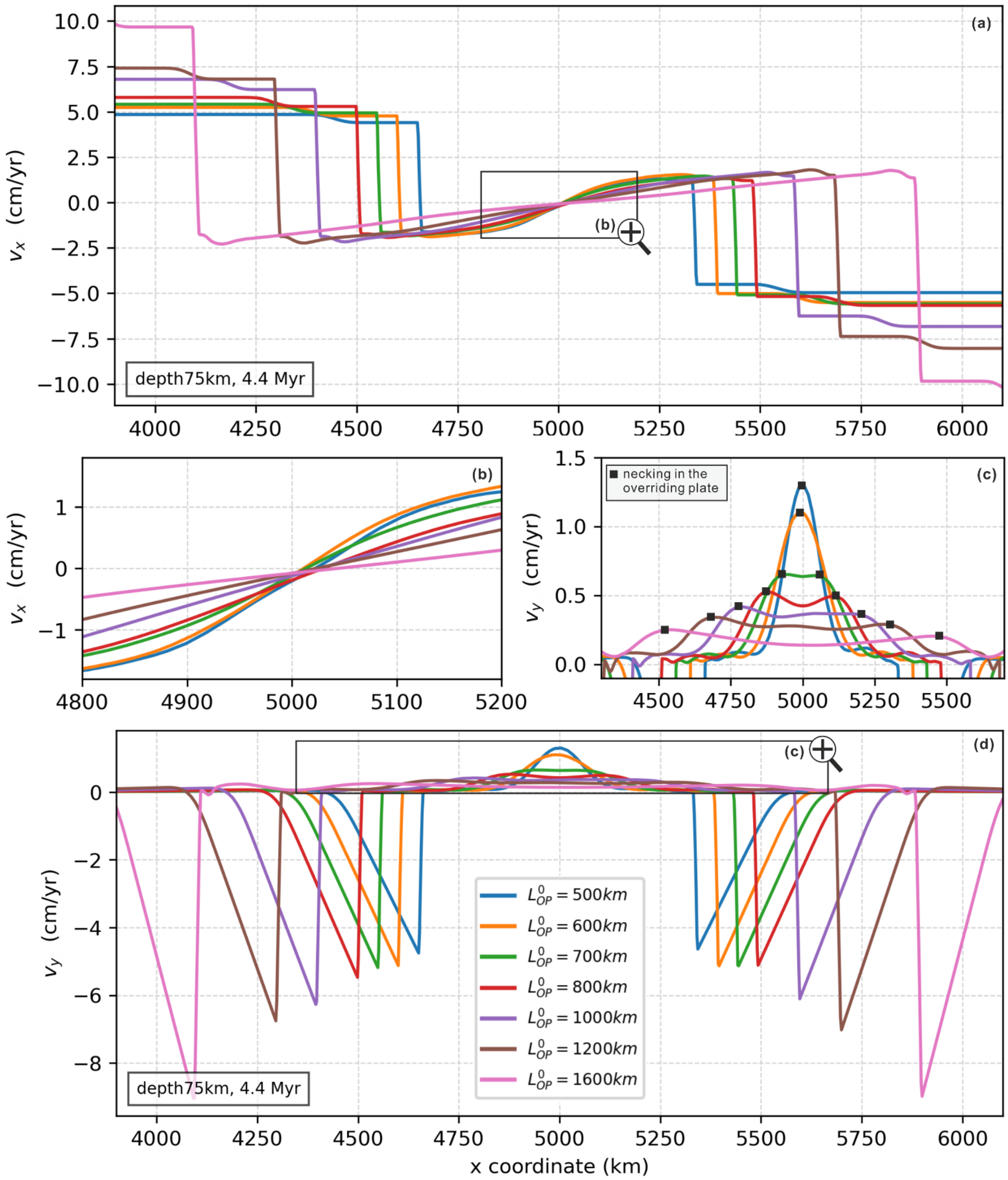

Figure 12. Velocity variation along a slice at the depth of 75 km, which is ~8 km below the 1300 K isotherm of the overriding plate, after 4.4 Myr simulation. (a, d) Horizontal and vertical component of velocity along the slice. (b) and (c) are zoom-in of (a) and (d) under the middle part of the overriding plate (5000 ± 200 km and 5000 ± 650 km away from the side boundaries respectively). Positive value means rightward or upward motion, and negative value represents leftward or downward motion. In (c), the horizontal coordinate of the necked region in the overriding plate is plotted as black square to visualize its spatial correlation with upwelling component of mantle wedge flow. All plots share the same legend listed in (d).

Previous research on subduction-induced continental breakup implies that spreading extension develops above where the upwelling mantle flow diverges, flow which creates the highest shear stress gradient at the bottom of the overriding plate (Dal Zilio et al., 2018). This does not fully agree with our simulation results with varying L_{OP}^{0}. The divergent return flow is defined as the place where v_x changes direction. It always lies under the middle part (~5000 km away from the side boundaries) of the overriding plate for all models (Figure 12, a). However, the weakening area does not always develop in the middle of the overriding plate, e.g., when $L_{OP}^{0} \geq 800\ km$. Instead, it correlates better in space with the highest upwelling mantle flow velocity (Figure 12, c). The lateral distance from the highest upwelling component to the nearest trench is measured (Figure 12, d), and it is noted that the distance remains relatively constant at ~370 km for all models at 4.4 Myr. This suggests that the wavelength of the slab induced mantle wedge flow is not related with varying L_{OP}^{0}.

An interesting observation is that the subducting slab's sinking velocity increases (t_{660} decreases) with longer L_{OP}^{0} (Table 3), while the poloidal mantle flow gets weaker and the maximum weakening level in the overriding plate decreases. From the perspective of energy conservation, all the dynamic processes, e.g., plate motion, mantle convection, internal deformation etc., originates from the potential energy of the subducting slabs. This implies that more of the potential energy transfers into kinetic energy of the subducting plates instead of being consumed as dissipation energy in the overriding plates, as L_{OP}^{0} increases.

4.2 Overriding plate weakening mechanism

As introduced in the methods, we applied composite rheology which incorporates four deformation mechanisms everywhere in the simulation domain. Here, the dominant deformation mechanism

(DDM) is defined as the rheology law that yields the minimum magnitude of viscosity at a certain point. We try to understand the temporal and spatial evolution of the DDM within the overriding plate, especially in the region where strain localisation takes place. Then we evaluate the contribution of each deformation mechanism in promoting strain localisation within the overriding plate.

4.2.1 Dominant deformation mechanism analysis

The reference model '$L_{OP}^{0} = 1200\ km$' with limited extension has shown that the DDM is stratified with yielding, Peierls creep and dislocation creep as the depth increases within the overriding plate (Figure 2, b). Here, we further investigate how the DDM evolves in models that develop rifting and spreading extension within the overriding plate, e.g., model '$H_{OP}^{0} = 70\ km$'. Therein, the temporal phases show that the DDM is also spatially layered (Figure 13), with yielding initially dominating from the surface to the depth of ~35 km, underlain by Peierls creep dominating for the next ~10 km and then dislocation creep dominating for ~25 km (Figure 13, b-d). Among all the DDM at different depths throughout the simulation, yielding is always the thickest and dislocation creep comes as the second. To be noted, the DDM of diffusion creep with limited area is observed around the bottom of the overriding plate during the initial plate weakening (Figure 13, b), and it is completely replaced by dislocation creep after 3.6 Myr. During the thinning process of the overriding plate, the deformation mechanism of Peierls creep gives way to yielding and dislocation creep as DDM (Figure 13, d-g). The replacement and interplay among different DDM will be discussed in the next subsection.

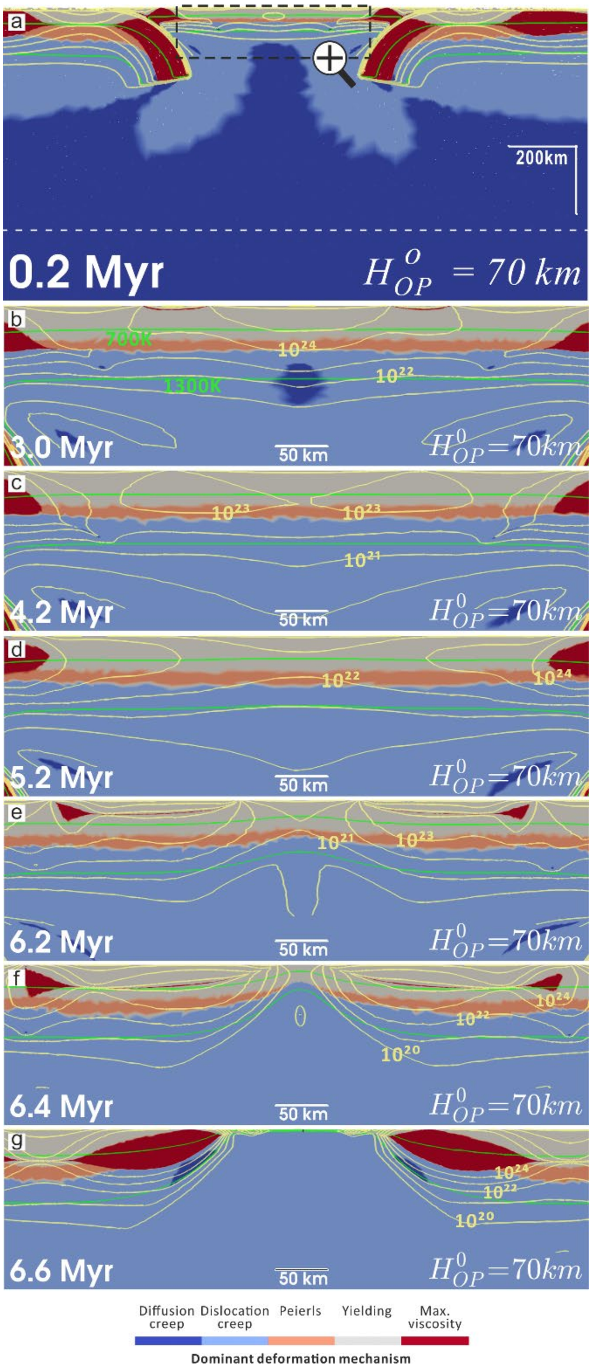

Figure 13. Temporal evolution of the dominant deformation mechanism within the overriding plate in model $H^{0}_{OP} = 70\ km$. The dashed zoom-in block in (a) shows the location of screenshots in (b-g). The progressive weakening process within the overriding plate is demonstrated by the necking of the iso-viscous contours. The 5 groups of yellow contours encompassing the plates in each screenshot are iso-viscous contours of $10^{20}, 10^{21}, 10^{22}, 10^{23}, 10^{24}\ Pa \cdot s$ from outward to inward. The two sets of green solid lines are 700 K and 1300 K isotherm contours to image the geometry of the thermal plate. The bottom left corner caption shows the elapsed simulation time and bottom right corner is the name of the model.

While we do not implement a multi-material approach to define the rheology of different layers in the lithosphere, the uniform compositional rheology law self-consistently generates the layered structure in Figure 13. In detail, yielding only dominates over other creep mechanisms in the cold regions, corresponding to the crustal depth range. While dislocation and diffusion creep dominate over yielding in the hot bottom region, equivalent to the depth range of mantle lithosphere. The continuous necking process shows that the viscosity reduction initiates from the surface (yielding) and the bottom of the plate (dislocation creep). Then the viscosity contour necks in the middle depth of the plate as seen in Figure 13, (b-e). This suggests that yielding and dislocation creep play the dominant role in promoting the continuous weakening of the overriding plate.

4.2.2 Weakening contribution analysis

The previous section has shown that the DDM may vary at different depth range within the overriding plate. To evaluate the contribution of each DDM to inducing rifting and spreading extension for each timestep, we slice the overriding plate vertically through its middle where the most intensive necking takes place. Then we group the points along the midline by the type of DDM. Two kinds of calculation are conducted. 1) For the points with the same DDM, we calculate at each timestep the arithmetic average of the strain rate and temperature state which can be used to compute the viscosity through Equation (8). 2) We compute the minimum viscosity among all points along the midline, and define the DDM that yields the minimum viscosity as the Minimum Viscosity Dominant Deformation Mechanism (MVDDM). To be clear, the DDM is calculated at each point independent of other points, while the MVDDM is calculated using all relevant points along the midline.

One diagnostic to evaluate the contribution of deformation mechanisms to plate weakening is to quantify how much (order of) viscosity reduction each DDM achieves. For model '$H_{OP}^{0} = 70\ km$', both yielding and dislocation creep reduces the viscosity to lower than $10^{21}\ Pa \cdot s$ (Figure 14, a), which is the critical magnitude to initiate rifting and spreading extension (Figure 7, a). While Peierls creep can reduce viscosity to the range of 10^{21}-10^{22} $Pa \cdot s$, which can enable limited thinning but it fails to induce rifting extension. Diffusion creep induces the least viscosity reduction to ~5×10^{22} $Pa \cdot s$, which suggests that it only softens the plate for further deformation through limited viscosity reduction. For models that do not develop rifting or spreading extension, the temporal paths of the DDM are similar with model '$H_{OP}^{0} = 70\ km$' except that the minimum viscosity is never less than 10^{21} $Pa \cdot s$. Another diagnostic to evaluate the contribution of deformation mechanisms to plate weakening is how long it stays active. We note that yielding and dislocation creep are two types of DDM that are active throughout the simulation (Figure 14, a), while diffusion creep and Peierls creep disappears as DDM along the midline after 3.6 Myr and 6.4 Myr separately (Figure 13, b, f).

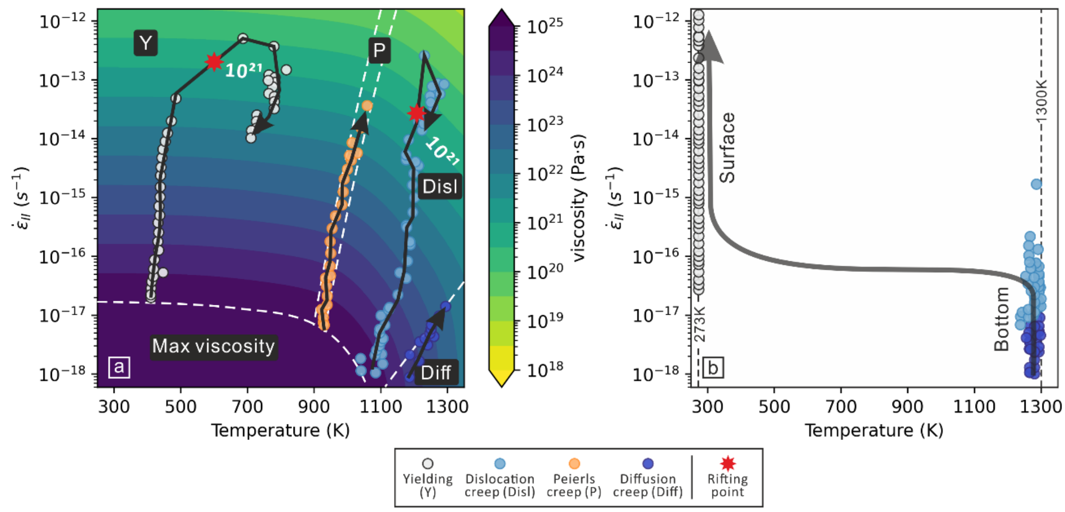

Figure 14. Scatter plots of the dominant deformation mechanism along the midline of the overriding plate (5000 km away from both side boundaries), i.e., the main necking region. (a) The temporal path of each dominant deformation mechanism (DDM) is plotted on a phase diagram, where the magnitude of viscosity is calculated based on Equation (7). The phase diagram is divided by the white dashed lines into four domains based on the calculation of which component deformation mechanism yields the minimum viscosity at the given strain rate, temperature and depth. The fifth domain marks the maximum viscosity. To be noted, the depth used to create the viscosity contour is 50 km, which may not reflect the complete temporal path but it helps to demonstrate how viscosity will evolve. The scatter points are taken from the model '$H_{OP}^{0} = 70\ km$', and each point is calculated by averaging the strain rate and temperature state at each timestep for the portion of the midline that holds the same dominant deformation mechanism. (b) The evolution of the dominant deformation mechanism that yields the minimum viscosity (MVDDM) throughout the midline of the overriding plate. Scatter points are taken from 5 models with varying thickness of the overriding plate (H_{OP}^{0}).

To be noted, we observe an accelerating viscosity reduction in the range of 10^{20}-$10^{22}\ Pa \cdot s$ for the DDM of yielding and dislocation creep (Figure 14, a). That is when plate thinning, rifting and spreading extension take place. The accelerating viscosity reduction suggests that the overriding plate falls into positive feedback weakening loops as strain localises in the necking region. Such self-strengthening weakening feedback loop when necking develops into a rifting centre is also reported in previous research using power-law viscous creeping flow law with an exponent > 1 (Wenker and Beaumont, 2018). As in the case of uniaxial stretching, the plate strength is proportional to $\bar{\mu} \times H_{OP}$ (Ribe, 2001), both of which in our models are reducing during the plate thinning process. Since the plate strength measures the very resistance to the underlying mantle flow, the reduction of viscosity and plate thickness will incur further plate weakening. The continuous plate strength reduction during dual inward dipping subduction may end up with the formation of new plate boundaries.

The location of the weakest point (with the least viscosity) along the midline migrates from the bottom of the overriding plate to the surface as dual inward dipping subduction proceeds (Figure 14, b). Correspondingly, the MVDDM changed from diffusion creep and dislocation creep at the bottom of the plate to yielding at the surface. Such a transition is observed no matter whether only rifting or full spreading extension develops within the overriding plate. The result indicates that the transition is enabled as long as the strain rate can keep increasing during subduction (Figure 14, b). Though, only a high enough strain rate (~$10^{-13}\ s^{-1}$) can lower the viscosity ($\sim 10^{21}\ Pa \cdot s$) sufficiently through yielding and dislocation creep to induce rifting and spreading extension (Figure 14, a).

While the rheology law (Equation (8-9)) of the four deformation mechanisms shows that the magnitude of viscosity is dependent on evolving temperature, strain rate, and lithostatic pressure, the diagram (Figure 14, a) indicates that the viscosity reduction is mainly driven by the ever-increasing strain rate relative to the much gentler impact of increasing thermal gradient and decreasing lithostatic pressure due to plate thinning. The dominant role of strain rate-induced weakening over thermal weakening is also reported in the interaction between upwelling plumes and overlying lithosphere (Burov and Guillou-Frottier, 2005). That is to say, the rheology and buoyancy parameters will be more important than the heat conduction parameters in producing different levels of rheology weakening within the overlying plate. The continuously growing strain rate can also explain the replacement of diffusion creep by dislocation creep as the DDM at the bottom of the overriding plate. While the replacement of Peierls creep by yielding or dislocation creep as DDM during the plate thinning process is likely due to both increasing strain rate and temperature at the intermediate depth. In addition, the strain rate induced weakening is also a precondition to initiate thermal weakening, lithosphere thinning, strain localisation and formation of new plate boundaries (eg. Fuchs and Becker, 2021, 2019; Gueydan et al., 2014).

4.3 Limitations

The major contribution of this work is incorporating a composite rheology which depends on multiple parameters, e.g., temperature, strain rate etc., for the dual inward dipping subduction models. However, previous research indicates that viscosity can also be affected by hydrous fluids, partial melting, and grain size of minerals in subduction zones (Bercovici et al., 2015; Braun et al., 1999; England and Katz, 2010; Montési and Hirth, 2003). In particular, grain size reduction is likely to take place when strain builds up and it may make diffusion creep become the dominant deformation mechanism, overtaking dislocation creep, in the mantle lithosphere (Gueydan et al., 2014; Ruh et al., 2022). Taking all these parameters into consideration is likely to strengthen the feedback weakening process within the overriding plate during dual inward dipping subduction, while at the cost of making the computation much more expensive (Foley, 2018).

Subduction can generate convective mantle flow that includes both poloidal and toroidal components. The 2D models tested here neglect the effects of toroidal flow and the third dimension. This could amplify the magnitude of poloidal flow and its weakening effect applied within the overriding plate. Considering that poloidal component dominates over toroidal component when slab subducts through the upper mantle (Funiciello et al., 2004), and it is the poloidal cell that provides the relevant traction driving the deformation within the overriding plate (Király et al., 2017; Schellart and Moresi, 2013), the lack of toroidal flow would only have limited impact on the progressive weakening presented.

Modern plate tectonic framework only provides limited examples of dual inward dipping subduction (see examples listed in introduction). Even though it is becoming more evident that dual inward dipping subduction also exists throughout plate tectonic history, the poor constraints on the state of paleo subduction zone systems, e.g., the thickness of the subducting and overriding plate, the distance between the trenches etc., makes an accurate and precise comparison with real-world or extinct dual inward dipping subduction zone very tricky. This research is designed as generic modelling rather than specific modelling. That is to say, the research does not try to match the results with any specific dual inward dipping subduction zone. Instead, it is designed to test the weakening potential dual inward dipping subduction can induce in the overriding plate under different model configuration.

Bearing all the limits in mind, we cautiously compare our model predictions with observations in the Caribbean Sea plate, which has experienced dual inward dipping subduction since at least ~60 Ma (Boschman et al., 2014; Braszus et al., 2021), with the Farallon plate (subsequently, Cocos and Nazca plates) subducting at the Central America Trench in the west and Proto-Caribbean plate (followed by Atlantic plate) subducting at the Lesser Antilles Trench in the east. One interesting observation from plate reconstruction is that the distance between the two trenches seems to have increased since the establishment of the dual inward dipping subduction (Barrera-Lopez et al., 2022; Boschman et al., 2014; Braszus et al., 2021; Romito and Mann, 2021), suggesting that the Caribbean plate has undergone extension. The extension includes the formation of multiple basins throughout the Caribbean Sea plate, e.g., Tobago Basin, Grenada Basin, Venezuela Basin and Colombia Basin since ~60 Ma (Allen et al., 2019; Braszus et al., 2021; Romito and Mann, 2021). The effect of the fixed boundary condition may play a role in promoting the extension, which may originate from the development of the Caribbean Large Igneous Province (Pindell et al., 2006), and multiple periods of back-arc extension as the Lesser Antilles Trench continuously retreats (Steel and Davison, 2021). We note that there is uncertainty in plate reconstructions and limited evidence on the timing of extension. Therefore, we must consider this comparison as somewhat speculative. Further the two-dimensional nature of the models might not be a good representation of the dynamics on the eastern side of the Caribbean plate with its narrow subduction zone.

4.4 Synoptic summary

The thermo-mechanical modelling here provides a generic understanding of the progressive weakening developed within a varying viscosity overriding plate during dual inward dipping subduction. To summarise, dual inward dipping subduction holds a stronger tendency to weaken the overriding plate compared with single sided subduction. This is achieved by creating a fixed trailing boundary condition for the overriding plate and generating a stronger poloidal return flow underlying the overriding plate (Figure 15). The stronger poloidal mantle flow is exhibited as a higher horizontal velocity gradient and higher maximum magnitude of upwelling component underlying the overriding plate. It can also initiate a higher degree of viscosity reduction, strain localisation and lithosphere thinning or even spreading extension within the overriding plate. Besides, a dual inward dipping subduction system with thinner and shorter overriding plate, and thicker subducting plate is likely to induce a higher degree of viscosity reduction within the overriding plate (Figure 15, b-d).

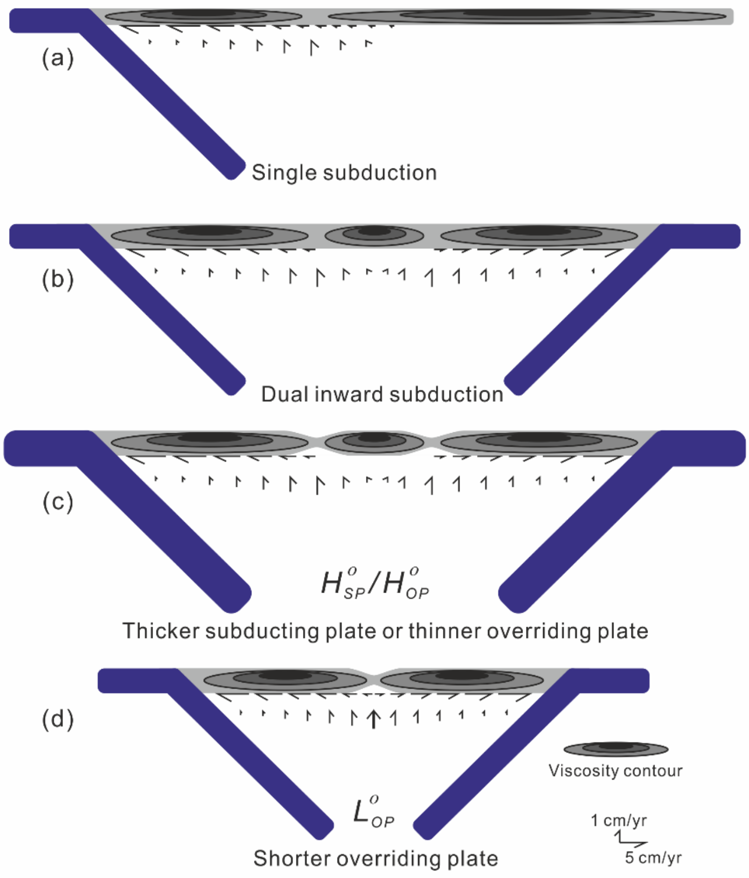

Figure 15. Synoptic comparison of different model setup's role in affecting the necking behaviour developed within the overriding plate. (a) Single sided subduction (Garel et al., 2014). (b) Dual inward dipping subduction. (c) Thickness of the subducting plate or overriding plate (H_{SP}^0, H_{OP}^0). (d) Length of the overriding plate (L_{OP}^0).

5. Conclusion

These 2-D thermo-mechanical numerical models demonstrate that dual inward dipping subduction can generate progressive weakening by lowering viscosity within the overriding plate on a ~10 Myr time scale. Three variables are investigated to understand what controls the maximum degree of weakening. It shows that the initial length (L_{OP}^0) and thickness (H_{OP}^0) of the overriding plate are negatively correlated with the maximum degree of weakening. While the initial thickness of the subducting plate (H_{SP}^0) positively relates to the maximum weakening level. The progressive weakening can result in a variety of irreversible stretching states ranging from 1) little or no lithosphere thinning and extension, to 2) limited thermal lithosphere thinning, and 3) localised rifting followed by spreading extension.

Comparing with single-sided subduction, dual inward dipping subduction can reduce the magnitude of viscosity to a lower level within the overriding plate. Two aspects are analysed. On the one hand, a dual inward dipping subduction set-up effectively creates a dynamic fixed boundary condition for the middle (overriding) plate. This inhibits the mobility of the plate and helps promote localised strain to accommodate the slab rollback tendency on both sides. On the other hand, when the initial length of the overriding plate is short enough ($L_{OP}^{0} \leq 800\ km$), dual inward dipping subduction can form a united upwelling mantle flow which interacts with the bottom of overriding plate and generates a stronger viscosity perturbation within it than single sided subduction models. As a result, dual inward dipping subduction can induce higher degrees of extension in the overriding plate compared with single sided subduction.

Yielding and dislocation creep are the dominant deformation mechanisms that initiates rifting and spreading extension. The progressive weakening is mainly driven by the ever-increasing strain rate, which is also a precondition for initiating thermal weakening, strain localisation, lithosphere thinning and formation of new plate boundaries.

Acknowledgement

We acknowledge the support of Advanced Research Computing at Cardiff (ARCCA) and the Supercomputing Wales project, which is part-funded by the European Regional Development Fund (ERDF) via the Welsh Government. Zhibin Lei also thanks the China Scholarship Council (CSC) for supporting the Ph.D. studentship and Cardiff University for an overseas fee waiver award.

References

Allen, R.W., Collier, J.S., Stewart, A.G., Henstock, T., Goes, S., Rietbrock, A., Macpherson, C., Blundy, J., Davidson, J., Harmon, N., Kendall, M., Prytulak, J., Rychert, C., Van Hunen, J., Wilkinson, J., Wilson, M., 2019. The role of arc migration in the development of the Lesser Antilles: A new tectonic model for the Cenozoic evolution of the eastern Caribbean. Geology 47, 891–895. https://doi.org/10.1130/G46708.1

Alsaif, M., Garel, F., Gueydan, F., Davies, D.R., 2020. Upper plate deformation and trench retreat modulated by subduction-driven shallow asthenospheric flows. Earth Planet. Sci. Lett. 532, 116013. https://doi.org/10.1016/j.epsl.2019.116013

Barrera-Lopez, C. V., Mooney, W.D., Kaban, M.K., 2022. Regional Geophysics of the Caribbean and Northern South America: Implications for Tectonics. Geochemistry, Geophys. Geosystems 23, 1–24. https://doi.org/10.1029/2021GC010112

Bercovici, D., Tackley, P.J., Ricard, Y., 2015. The Generation of Plate Tectonics from Mantle Dynamics, in: Treatise on Geophysics: Second Edition. Elsevier B.V., Oxford, pp. 271–318. https://doi.org/10.1016/B978-0-444-53802-4.00135-4

Boschman, L.M., van Hinsbergen, D.J.J., Torsvik, T.H., Spakman, W., Pindell, J.L., 2014. Kinematic reconstruction of the caribbean region since the early jurassic. Earth-Science Rev. 138, 102–136. https://doi.org/10.1016/j.earscirev.2014.08.007

Braszus, B., Goes, S., Allen, R., Rietbrock, A., Collier, J., Harmon, N., Henstock, T., Hicks, S., Rychert, C.A., Maunder, B., van Hunen, J., Bie, L., Blundy, J., Cooper, G., Davy, R., Kendall, J.M., Macpherson, C., Wilkinson, J., Wilson, M., 2021. Subduction history of the Caribbean from upper-mantle seismic imaging and plate reconstruction. Nat. Commun. 12. https://doi.org/10.1038/s41467-021-24413-0

Braun, J., Chéry, J., Poliakov, A., Mainprice, D., Vauchez, A., Tomassi, A., Daignières, M., 1999. A simple parameterization of strain localization in the ductile regime due to grain size reduction: A case study for olivine. J. Geophys. Res. Solid Earth 104, 25167–25181.

Bürgmann, R., Dresen, G., 2008. Rheology of the lower crust and upper mantle: Evidence from rock mechanics, geodesy, and field observations. Annu. Rev. Earth Planet. Sci. 36, 531–567. https://doi.org/10.1146/annurev.earth.36.031207.124326

Burov, E., Guillou-Frottier, L., 2005. The plume head-continental lithosphere interaction using a tectonically realistic formulation for the lithosphere. Geophys. J. Int. 161, 469–490. https://doi.org/10.1111/j.1365-246X.2005.02588.x

Burov, E.B., 2011. Rheology and strength of the lithosphere. Mar. Pet. Geol. 28, 1402–1443. https://doi.org/10.1016/j.marpetgeo.2011.05.008

Byerlee, J., 1978. Friction of rocks. Pure Appl. Geophys. PAGEOPH 116, 615–626. https://doi.org/10.1007/BF00876528

Capitanio, F.A., Stegman, D.R., Moresi, L.N., Sharples, W., 2010. Upper plate controls on deep subduction, trench migrations and deformations at convergent margins. Tectonophysics 483, 80–92. https://doi.org/10.1016/j.tecto.2009.08.020

Chen, Z., Schellart, W.P., Strak, V., Duarte, J.C., 2016. Does subduction-induced mantle flow drive backarc extension? Earth Planet. Sci. Lett. 441, 200–210. https://doi.org/10.1016/j.epsl.2016.02.027

Chertova, M. V., Geenen, T., Van Den Berg, A., Spakman, W., 2012. Using open sidewalls for modelling self-consistent lithosphere subduction dynamics. Solid Earth 3, 313–326. https://doi.org/10.5194/se-3-313-2012

Čížková, H., Bina, C.R., 2013. Effects of mantle and subduction-interface rheologies on slab stagnation and trench rollback. Earth Planet. Sci. Lett. 379, 95–103. https://doi.org/10.1016/j.epsl.2013.08.011

Crameri, F., Tackley, P.J., Meilick, I., Gerya, T. V., Kaus, B.J.P., 2012. A free plate surface and weak oceanic crust produce single-sided subduction on Earth. Geophys. Res. Lett. 39, 1–7. https://doi.org/10.1029/2011GL050046

Dal Zilio, L., Faccenda, M., Capitanio, F., 2018. The role of deep subduction in supercontinent breakup. Tectonophysics 746, 312–324. https://doi.org/10.1016/j.tecto.2017.03.006

Dasgupta, R., Mandal, N., 2018. Surface topography of the overriding plates in bi-vergent subduction systems: A mechanical model. Tectonophysics 746, 280–295. https://doi.org/10.1016/j.tecto.2017.08.008

Davies, D.R., Wilson, C.R., Kramer, S.C., 2011. Fluidity: A fully unstructured anisotropic adaptive mesh computational modeling framework for geodynamics. Geochemistry, Geophys. Geosystems 12, n/a-n/a. https://doi.org/10.1029/2011GC003551

Di Giuseppe, E., Van Hunen, J., Funiciello, F., Faccenna, C., Giardini, D., 2008. Slab stiffness control of trench motion: Insights from numerical models. Geochemistry, Geophys. Geosystems 9, 1–19. https://doi.org/10.1029/2007GC001776

England, P.C., Katz, R.F., 2010. Melting above the anhydrous solidus controls the location of volcanic arcs. Nature 467, 700–703. https://doi.org/10.1038/nature09417

Erdős, Z., Huismans, R.S., Faccenna, C., Wolf, S.G., 2021. The role of subduction interface and upper plate strength on back-arc extension: Application to Mediterranean back-arc basins. Tectonics 40. https://doi.org/10.1029/2021TC006795

Faccenna, C., Becker, T.W., Holt, A.F., Brun, J.P., 2021. Mountain building, mantle convection, and supercontinents: Holmes (1931) revisited. Earth Planet. Sci. Lett. 564, 116905. https://doi.org/10.1016/j.epsl.2021.116905

Faccenna, C., Becker, T.W., Lallemand, S., Lagabrielle, Y., Funiciello, F., Piromallo, C., 2010. Subduction-triggered magmatic pulses: A new class of plumes? Earth Planet. Sci. Lett. 299, 54–68. https://doi.org/10.1016/j.epsl.2010.08.012

Foley, B.J., 2018. On the dynamics of coupled grain size evolution and shear heating in lithospheric shear zones. Phys. Earth Planet. Inter. 283, 7–25. https://doi.org/10.1016/j.pepi.2018.07.008

Fowler, C., 2005. The Solid Earth: An Introduction to Global Geophysics. Cambridge Univ. Press, Cambridge, U. K.

Fuchs, L., Becker, T.W., 2021. Deformation memory in the lithosphere: A comparison of damage-dependent weakening and grain-size sensitive rheologies. J. Geophys. Res. Solid Earth 126, 1–22. https://doi.org/10.1029/2020JB020335

Fuchs, L., Becker, T.W., 2019. Role of strain-dependent weakening memory on the style of mantle convection and plate boundary stability. Geophys. J. Int. 218, 601–618. https://doi.org/10.1093/gji/ggz167

Funiciello, F., Faccenna, C., Giardini, D., 2004. Role of lateral mantle flow in the evolution of subduction systems: Insights from laboratory experiments. Geophys. J. Int. 157, 1393–1406. https://doi.org/10.1111/j.1365-246X.2004.02313.x

Garel, F., Goes, S., Davies, D.R., Davies, J.H., Kramer, S.C., Wilson, C.R., 2014. Interaction of subducted slabs with the mantle transition-zone: A regime diagram from 2-D thermo-mechanical models with a mobile trench and an overriding plate. Geochemistry, Geophys. Geosystems 15, 1739–1765. https://doi.org/10.1002/2014GC005257

Garel, F., Thoraval, C., 2021. Lithosphere as a constant-velocity plate: Chasing a dynamical LAB in a homogeneous mantle material. Phys. Earth Planet. Inter. 316, 106710. https://doi.org/10.1016/j.pepi.2021.106710

Gerardi, G., Ribe, N.M., 2018. Boundary Element Modeling of Two-Plate Interaction at Subduction Zones: Scaling Laws and Application to the Aleutian Subduction Zone. J. Geophys. Res. Solid Earth 123, 5227–5248. https://doi.org/10.1002/2017JB015148

Gerya, T. V., Connolly, J.A.D., Yuen, D.A., 2008. Why is terrestrial subduction one-sided? Geology 36, 43–46. https://doi.org/10.1130/G24060A.1

Gueydan, F., Précigout, J., Montési, L.G.J., 2014. Strain weakening enables continental plate tectonics. Tectonophysics 631, 189–196. https://doi.org/10.1016/j.tecto.2014.02.005

Gülcher, A.J.P., Gerya, T. V., Montési, L.G.J., Munch, J., 2020. Corona structures driven by plume–lithosphere interactions and evidence for ongoing plume activity on Venus. Nat. Geosci. 13, 547–554. https://doi.org/10.1038/s41561-020-0606-1

Hall, R., Spakman, W., 2015. Mantle structure and tectonic history of SE Asia. Tectonophysics 658, 14–45. https://doi.org/10.1016/j.tecto.2015.07.003

Hirth, G., Kohlstedt, D., 2003. Rheology of the upper mantle and the mantle wedge: A view from the experimentalists, in: Eiler, J. (Ed.), Inside the Subduction Factory. American Geophysical Union, pp. 83–105. https://doi.org/10.1029/138GM06

Hirth, G., Kohlstedt, D.L., 1995a. Experimental constraints on the dynamics of the partially molten upper mantle: Deformation in the diffusion creep regime. J. Geophys. Res. Solid Earth 100, 1981–2001. https://doi.org/https://doi.org/10.1029/94JB02128

Hirth, G., Kohlstedt, D.L., 1995b. Experimental constraints on the dynamics of the partially molten upper mantle 2. Deformation in the dislocation creep regime. J. Geophys. Res. 100, 1981–2001. https://doi.org/10.1029/95jb01292

Holt, A.F., Becker, T.W., Buffett, B.A., 2015. Trench migration and overriding plate stress in dynamic subduction models. Geophys. J. Int. 201, 172–192. https://doi.org/10.1093/gji/ggv011

Holt, A.F., Royden, L.H., Becker, T.W., 2017. The Dynamics of Double Slab Subduction. Geophys. J. Int. 209, ggw496. https://doi.org/10.1093/gji/ggw496

Huang, Z., Zhao, D., Wang, L., 2015. P wave tomography and anisotropy beneath Southeast Asia: Insight into mantle dynamics. J. Geophys. Res. Solid Earth 120, 5154–5174. https://doi.org/10.1002/2015JB012098

Kameyama, M., Yuen, D.A., Karato, S.I., 1999. Thermal-mechanical effects of low-temperature plasticity (the Peierls mechanism) on the deformation of a viscoelastic shear zone. Earth Planet. Sci. Lett. 168, 159–172. https://doi.org/10.1016/S0012-821X(99)00040-0

Karato, S. ichiro, 2010. Rheology of the Earth’s mantle: A historical review. Gondwana Res. 18, 17–45. https://doi.org/10.1016/j.gr.2010.03.004

Király, Á., Capitanio, F.A., Funiciello, F., Faccenna, C., 2017. Subduction induced mantle flow: Length-scales and orientation of the toroidal cell. Earth Planet. Sci. Lett. 479, 284–297. https://doi.org/10.1016/j.epsl.2017.09.017

Király, Á., Funiciello, F., Capitanio, F.A., Faccenna, C., 2021. Dynamic interactions between subduction zones. Glob. Planet. Change 202, 103501. https://doi.org/10.1016/j.gloplacha.2021.103501

Kramer, S.C., Wilson, C.R., Davies, D.R., 2012. An implicit free surface algorithm for geodynamical simulations. Phys. Earth Planet. Inter. 194–195, 25–37. https://doi.org/10.1016/j.pepi.2012.01.001

Kreemer, C., Blewitt, G., Klein, E.C., 2014. A geodetic plate motion and Global Strain Rate Model. Geochemistry, Geophys. Geosystems 15, 3849–3889. https://doi.org/10.1002/2014GC005407

Lynch, H.D., Morgan, P., 1987. The tensile strength of the lithosphere and the localization of extension. Geol. Soc. Spec. Publ. 28, 53–65. https://doi.org/10.1144/GSL.SP.1987.028.01.05

Lyu, T., Zhu, Z., Wu, B., 2019. Subducting slab morphology and mantle transition zone upwelling in double-slab subduction models with inward-dipping directions. Geophys. J. Int. 218, 2089–2105. https://doi.org/10.1093/gji/ggz268

Maruyama, S., Santosh, M., Zhao, D., 2007. Superplume, supercontinent, and post-perovskite: Mantle dynamics and anti-plate tectonics on the Core-Mantle Boundary. Gondwana Res. 11, 7–37. https://doi.org/10.1016/j.gr.2006.06.003

McKenzie, D.P., Roberts, J.M., Weiss, N.O., 1974. Convection in the earth's mantle: towards a numerical simulation. J. Fluid Mech. 62, 465. https://doi.org/10.1017/S0022112074000784

Montési, L.G.J., Hirth, G., 2003. Grain size evolution and the rheology of ductile shear zones: From laboratory experiments to postseismic creep. Earth Planet. Sci. Lett. 211, 97–110. https://doi.org/10.1016/S0012-821X(03)00196-1

Nakakuki, T., Mura, E., 2013. Dynamics of slab rollback and induced back-arc basin formation. Earth Planet. Sci. Lett. 361, 287–297. https://doi.org/10.1016/j.epsl.2012.10.031

Perfit, M.R., Gust, D.A., Bence, A.E., Arculus, R.J., Taylor, S.R., 1980. Chemical characteristics of island-arc basalts: Implications for mantle sources. Chem. Geol. 30, 227–256. https://doi.org/10.1016/0009-2541(80)90107-2

Pindell, J., Kennan, L., Stanek, K.P., Maresch, W. V., Draper, G., 2006. Foundations of Gulf of Mexico and Caribbean evolution: Eight controversies resolved. Geol. Acta 4, 303–341.

Ranalli, G., 1995. Rheology of the Earth. Springer Science & Business Media.

Ribe, N.M., 2001. Bending and stretching of thin viscous sheets. J. Fluid Mech. 433, 135–160. https://doi.org/10.1017/S0022112000003360

Romito, S., Mann, P., 2021. Tectonic terranes underlying the present-day Caribbean plate: their tectonic origin, sedimentary thickness, subsidence histories and regional controls on hydrocarbon resources, in: Davison, I., Hull, J.N.F., Pindell, J. (Eds.), The Basins, Orogens and Evolution of the Southern Gulf of Mexico and Northern Caribbean. Geological Society of London, p. 0. https://doi.org/10.1144/SP504-2019-221

Ruh, J.B., Tokle, L., Behr, W.M., 2022. Grain-size-evolution controls on lithospheric weakening during continental rifting. Nat. Geosci. https://doi.org/10.1038/s41561-022-00964-9

Santosh, M., 2010. Assembling North China Craton within the Columbia supercontinent: The role of double-sided subduction. Precambrian Res. 178, 149–167. https://doi.org/10.1016/j.precamres.2010.02.003

Schellart, W.P., Moresi, L., 2013. A new driving mechanism for backarc extension and backarc shortening through slab sinking induced toroidal and poloidal mantle flow: Results from dynamic subduction models with an overriding plate. J. Geophys. Res. Solid Earth 118, 3221–3248. https://doi.org/10.1002/jgrb.50173

Schliffke, N., van Hunen, J., Allen, M.B., Magni, V., Gueydan, F., 2022. Episodic back-arc spreading centre jumps controlled by transform fault to overriding plate strength ratio. Nat. Commun. 13, 582. https://doi.org/10.1038/s41467-022-28228-5

Sleep, N.H., Toksöz, M.N., 1971. Evolution of Marginal Basins. Nature 233, 548–550. https://doi.org/10.1038/233548a0

Steel, I., Davison, I., 2021. Explanatory note: Map of the geology of the northern caribbean and the greater antillean arc. Geol. Soc. Spec. Publ. 504, 1–2. https://doi.org/10.1144/SP504-2020-3

Straub, S.M., Gómez-Tuena, A., Vannucchi, P., 2020. Subduction erosion and arc volcanism. Nat. Rev. Earth Environ.

1, 574–589. https://doi.org/10.1038/s43017-020-0095-1

Suchoy, L., Goes, S., Maunder, B., Garel, F., Davies, R., 2021. Effects of basal drag on subduction dynamics from 2D numerical models. Solid Earth 12, 79–93. https://doi.org/10.5194/se-12-79-2021

Turcotte, D., Schubert, G., 2014. Geodynamics, 3rd ed. Cambridge University Press, Cambridge. https://doi.org/10.1017/CBO9780511843877

Uyeda, S., 1981. Subduction zones and back arc basins — A review. Geol. Rundschau 70, 552–569. https://doi.org/10.1007/BF01822135

Van Benthem, S., Govers, R., Spakman, W., Wortel, R., 2013. Tectonic evolution and mantle structure of the Caribbean. J. Geophys. Res. Solid Earth 118, 3019–3036. https://doi.org/10.1002/jgrb.50235

van der Meer, D.G., van Hinsbergen, D.J.J., Spakman, W., 2018. Atlas of the underworld: Slab remnants in the mantle, their sinking history, and a new outlook on lower mantle viscosity. Tectonophysics 723, 309–448. https://doi.org/10.1016/j.tecto.2017.10.004

Wenker, S., Beaumont, C., 2018. Effects of lateral strength contrasts and inherited heterogeneities on necking and rifting of continents. Tectonophysics 746, 46–63. https://doi.org/10.1016/j.tecto.2016.10.011

Windley, B.F., Maruyama, S., Xiao, W.J., 2010. Delamination/thinning of sub-continental lithospheric mantle under eastern China: The role of water and multiple subduction. Am. J. Sci. 310, 1250–1293. https://doi.org/10.2475/10.2010.03

Yang, T., Moresi, L., Gurnis, M., Liu, S., Sandiford, D., Williams, S., Capitanio, F.A., 2019. Contrasted East Asia and South America tectonics driven by deep mantle flow. Earth Planet. Sci. Lett. 517, 106–116. https://doi.org/10.1016/j.epsl.2019.04.025